

Three Dimensional Independent Control of Multiple Magnetic Microrobots via Inter-Agent Forces

Mohammad Salehizadeh¹ and Eric Diller¹

Abstract

This paper presents a method to independently control the position of multiple microscale magnetic robots in 3D, operating in close proximity to each other. Having multiple magnetic microrobots work together in close proximity is difficult due to magnetic interactions between the robots, and here we aim to control those interactions for the creation of desired multi-agent formations in 3D. Based on the fact that all magnetic agents orient to the global input magnetic field, the local attraction-repulsion forces between nearby agents can be regulated. For the first time, 3D manipulation of two microgripping magnetic microrobots is demonstrated. We also mathematically and experimentally prove that the center-of-mass external magnetic pulling of the multi-agent system is possible in 3D with an underactuated magnetic field generator. Here we utilize the controlled interaction magnetic forces between two spherical agents to steer them along two prescribed paths. We apply our method to independently control the motion of a pair of magnetic microgrippers as functional microrobot candidates each equipped with a 5 degree of freedom motion mechanism and a grasp-release mechanism for targeted cargo delivery. A proportional controller and an optimization-based controller are introduced and compared, with potential to control more than two magnetic agents in 3D. Average tracking errors of less than 141 and 165 micrometers are accomplished for the regulation of agents' positions using optimization-based and proportional controllers, respectively, for spherical agents with approximate nominal radius of 500 micrometers operating within several body-lengths of each other.

Keywords

microrobotics, multi-agent control at small scales, underactuated robotics, 3D micromanipulation, targeted cargo delivery, multi-functional robotics, microgripper

1 Introduction

A microrobot agent is a small-scale robot with characteristic dimensions less than 1 mm. Microrobots of simple construction have been explored powered by a number of different actuation methods for medical applications including targeted drug delivery, wireless sampling and microsurgery.

Among many proposed strategies, magnetic actuation has been recognized as a good choice for hard-to-reach 3D environments especially inside the human body (Ceylan et al. 2017) due to its capability to remotely generate strong torques and forces on magnetic materials in 3D (Zhang et al. 2012), and is safe to generate and manipulate for dexterous manipulation (Kummer et al. 2010). The capability to use multiple microrobots operating in parallel has the potential to increase payload capacity in drug delivery or sampling applications, gaining a better visibility during in-vivo imaging, and increasing task speed in pick-and-place manipulation.

Toward magnetic control of teams of mobile microrobots, a variety of approaches have been investigated. To name a few, fluidic interactions are considered to achieve dynamic self-assembly of objects energized by electric or magnetic fields (Yu et al. 2018; Xie et al. 2019; Kaiser et al. 2017; Kokot et al. 2015; Salehizadeh et al. 2019). These particles rotate at a liquid-air interface with complex motions that are not possible with conventional systems. Arrays of planar addressing micro-coil arrays were employed to construct

discrete plans throughout an optimal control algorithm to do manipulation of multiple magnetic microrobots (Kantaros et al. 2018). A common drawback of these methods is that they are all limited to 2D applications.

In the same spirit, swarm control of large numbers of microrobots has been thoroughly investigated by simultaneous steering of identical microrobots utilizing a uniform (Yu et al. 2018) and nonuniform (Dong and Sitti 2020) magnetic field. Nevertheless, independent control of each member of such a large swarm remains elusive as in most actuation systems, all magnetic microrobots receive identical control inputs and thus may not be steered independently for complex task completion (Chowdhury et al. 2015; Rubenstein et al. 2014). Authors in (Abbott et al. 2017) derived a general compact analytic approach using linear-algebraic representations to find a minimum-power dipole solution for a given set of desired interdipole forces with application to electromagnetic formation flight. However, their approach may not be applicable to microrobotic system which is heavily

¹ Department of Mechanical and Industrial Engineering, University of Toronto, Canada

Corresponding author:

Eric Diller, Microrobotics Laboratory, Department of Mechanical and Industrial Engineering, University of Toronto, 5 King's College Road, Toronto, Ontario, M5S 3G8, Canada
Email: ediller@mie.utoronto.ca

Class 1	Class 2		Class 3	
based on spatial position of agents once exposed to a patterned input magnetic field (Rahmer et al. 2017); (Wong et al. 2016); (Dong and Sitti 2020); (Johnson et al. 2020); (Chowdhury et al. 2017)	based on heterogeneity of agents realized by (see belows for subclasses):		based on direct field actuation formed by (see below for subclasses):	
	(a)	geometrically distinct microrobots: including (Diller et al. 2013); (Tottori et al. 2013), or agents' tail response to fluid drag (Khalil et al. 2018)	(a)	external magnetic pulling-only action via nonuniform field actuation (Ongaro et al. 2019)
	(b)	magnetically distinct microrobots: through their selective response to the pulsing frequency of the applied magnetic fields (Floyd et al. 2011); (Diller et al. 2011); using microrobots with unique step-out or natural frequencies (Howell et al. 2018); (Huang et al. 2014), exploiting difference in agents' turning rate (Becker et al. 2014), or difference in magnetic hysteresis (Miyashita et al. 2013)	(b)	homogeneous quasi-static field (Salehizadeh et al. 2018)
			(i)	fully actuated system: operated by direct independent magnetic actuation of multiple degrees-of-freedom (DOFs) (Diller et al. 2016); (Salmanipour and Diller 2018)
		(ii)	underactuated system: operated by inter-agent forces between multiple magnetic agents (Salehizadeh and Diller 2016); (Salehizadeh and Diller 2017b,a); (Zhang et al. 2018); (Choi et al. 2017)	

Fig. 1. Multi-agent strategies used by existing studies with classification toward independent control of multiple magnetic microrobots.

underactuated and the relation between coil currents and inter-dipole forces is not always linear.

The ability to exert independent control over a team of magnetic microrobots has the potential to enable precision operations, especially for dexterous tasks requiring microrobots with on-board tools to precisely pick or deliver cargo such as biopsy samples or drugs. Therefore, it is essential to customize the system magnetic response for each agent in the team. In this context, several approaches have been explored toward the independent control of multiple magnetic microrobots that can be classified into three classes, depending on how their control is constructed (see Fig. 1).

The drawback of class 1 is that to get the best output from this class: agents are required to be identical; the static task volume is limited and selective which makes it hard to generalize the class dynamically; and the existing inter-agent radial and rotational force primitives contributing to the motion are ignored. Class 2 relies on heterogeneity requirement as the control basis, which may limit the practical application and scalability of the method. Class 3 does not directly rely upon agents' diversity, hence has a stronger potential that can be flexibly generalized to 3D and a larger number of agents. In the pulling-only method 3(a), the authors designed a highly dexterous electromagnetic coil system by which they can independently control the position of two mobile magnetic microrobots in 3D using magnetic gradient pulling only. That system is capable of generating independent pulling forces on each of two magnetic agents. The technique requires solution of a complex nonlinear problem requiring a significant computational effort and a suitable thermal management system to prevent the powerful electromagnets from overheating.

The key advantage of method 3(b) stems from the fact that it simply relies upon "homogeneous quasi-static" field—a term that is used to describe a field which is spatially uniform and constant over short time periods. This requirement makes the approach a suitable fit specifically for applications inside the human body, where the coils have to stay far apart over a distance much larger than the distance between agents. This condition makes the generation of homogeneous field to be effectively easier as opposed to the pulling-only method 3(a) that requires a nonuniform field generator with large field gradient. One can classify class 3(b) itself into two groups: i) fully actuated, and ii) underactuated systems. To realize a fully actuated magnetic system, the overall actuation matrix which relates the system inputs to the output DOFs must be made full-rank. On the other hand, for underactuated magnetic systems such as when multiple magnetic microrobots mutually interact with each other in close proximity it is crucial to use underactuated robotics techniques. These types of systems will become inherently underactuated especially as the number of agents scales up. The control of agents motion in such underactuated systems is the main focus of this paper (highlighted in Fig. 1).

Another major challenge with the team control of magnetic microrobots is that strong magnetic inter-agent forces are present which tend to cause the microrobots to irreversibly attract and stick together. Previous studies either ignored these inter-agent forces by simply assuming their robots are adequately far apart, or treat these forces as a system disturbance without verifying the stability in close proximity. Nonetheless, if one can understand, model and control the coupled motion of magnetic agents, deterministic locomotion of the collective robotic team can be achieved, much as happens in living swarms of organisms (Li et al. 2019).

Our study provides understanding of the inter-agent forces for microrobots operating in close proximity and introduces methods to control the forces to exert additional control of the team.

Our previous studies (Salehizadeh and Diller 2016, 2017b,a; Zhang et al. 2018) introduced the inter-agent force method 3(b)-ii to control the motion of two or more spherical and functional agents in close proximity in 2D using homogeneous magnetic field by posing the system as an underactuated first-order kinematic motion problem. We hypothesize in this paper that use of magnetic inter-agent forces can be generalized to achieve 3D manipulation of a pair of mobile magnetic microrobots in close proximity without letting them touch each other. In this paper, we validate this hypothesis.

Given that there can be no stable magnetic equilibrium point in a static magnetic field based on Earnshaw's theorem, it can be concluded that any system designed to manipulate untethered levitating magnetic agents must use feedback control to stabilize the position of the agents (Abbott et al. 2020). The main contribution of this paper is that it discovers the impact of magnetic inter-agent forces on 3D motion of multiple magnetic microrobots while manipulated by an underactuated system, based on which controllers are synthesized and validated to independently regulate the position of both types of particle and functional microrobots. Our method incorporates an applied global magnetic field which not only controls the global center-of-mass (COM) position and grasp/release action of microgrippers, but also modulates the local magnetic interaction between microrobots responsible for the regulation of the agents' relative positions. In addition, we demonstrate mathematically and experimentally that external magnetic pulling of multiple magnetic microrobots at various range of separations is possible in 3D using a magnetic generator with a rank-deficient actuation matrix. Lastly, we generalize the definition of our control principle in the form of an optimization-based controller (OBC) which has potential to control more magnetic agents in 3D. Our experimental demonstrations include three parts: 1) Path tracking of two microspheres in 3D. 2) Implementing the idea of inter-agent forces to functional microrobots in the shape of grippers to perform 3D cargo delivery. 3) A 3D experimental comparison of two types of controllers for a two-agent team.

The key attributes of the multi-agent control method presented in this paper are as follows:

1. It offers a 3D solution to multi-agent magnetic control by taking benefit from inter-agent forces to control the motion of agents in close proximity. The presented approach is invariant to the magnetic manipulation system used and thus the results presented here could be repeated in a wide variety of microrobotic magnetic manipulations systems which can create a magnetic field in an arbitrary direction.
2. The approach does not depend on whether the field generation coils are far or close from the workspace, can be applied to microrobots with either soft (non-permanent) or hard (permanent) magnets, which are all identical or nonidentical.

3. Since the method only relies on the orientation of the applied magnetic field, in addition one could benefit at the same time from other aspects of the uniform field such as its magnitude and frequency to build multimodal field-activated medical devices or to run cooperative drug delivery tasks (Salehizadeh et al. 2019; Zhang et al. 2018; Wang et al. 2018).
4. Small-scale devices which consist of multiple magnetic actuators suffer from cross-talk in their functions mainly due to inter-magnet forces (Salmanipour and Diller 2018). The underlying method in this paper can be engaged to eliminate those cross-talks by making full use of inter-agent forces that get pronounced over small separations.

The paper is structured as follows. Section 2 describes the 3D kinematics of agents along with the inter-agent force relation. Section 3 introduces our control principles to regulate the relative motion of agents; accordingly, a systematic feedback control law is synthesized to handle best performance. Next, fabrication method and experimental setup are presented in Section 4. The paper ends in Section 5 with experimental results demonstrating the independent position control of a pair of magnetic microrobots. This paper is concluded in Section 6.

2 Concepts and definitions

This section introduces the 3D kinematics describing a pair of magnetic agents along with the inter-agent force relation, and lays the foundation for controlling a two-agent configuration in 3D.

2.1 Force and torque on a magnetic agent

We begin the problem formulation by reviewing the relevant background. In the presence of magnetic field vector \mathbf{b} generated by another source, a magnetic agent characterized by magnetic moment \mathbf{m} is compelled to translate and rotate in an attempt to minimize magnetic energy $(-\mathbf{b} \cdot \mathbf{m})$. As a result the magnetic agent will experience a torque which tends to rotate the agent into alignment with the field, and a force which pulls the agent according to the shape of the magnetic field. The magnetic force can be expressed linearly with respect to \mathbf{m} (Abbott et al. 2020):

$$\mathbf{f}_{3 \times 1} = \nabla(\mathbf{b} \cdot \mathbf{m}) = \underbrace{\begin{bmatrix} \frac{db}{dx} & \frac{db}{dy} & \frac{db}{dz} \end{bmatrix}}_{\mathbb{B}_\nabla} \mathbf{m} \quad (1)$$

The spatial field-derivative matrix above is denoted by \mathbb{B}_∇ which is symmetric with a trace of zero based on Maxwell's equation (Petruska and Nelson 2015). The magnetic torque $\boldsymbol{\tau}$ can be expressed as

$$\boldsymbol{\tau}_{3 \times 1} = \mathbf{m} \times \mathbf{b} = \mathbb{S}\{\mathbf{m}\}\mathbf{b}. \quad (2)$$

Where the function $\mathbb{S}\{\mathbf{m}\}$ indicates the skew-symmetric matrix packing of vector \mathbf{m} . Note that it is impossible for a single magnetic agent to generate torque about the \mathbf{m} axis, regardless of the magnetic field. This constrains force-torque generation on a magnetic agent to 5 degrees of freedom (DOF) (Mahoney and Abbott 2016).

2.2 Force and torque between a pair of magnetic agents

The force imparted on a magnetic agent m_j at location P_j from the field derivative $\mathbb{B}_\nabla\{P_j, m_i, P_i\}$ associated to another magnetic agent m_i is:

$$f_{ij} = \frac{3\mu_0}{4\pi\|r_{ij}\|^4} \left((\hat{r}_{ij}^\top m_j) m_i + (\hat{r}_{ij}^\top m_i) m_j + \left(m_i^\top m_j - 5 (\hat{r}_{ij}^\top m_i) (\hat{r}_{ij}^\top m_j) \right) \hat{r}_{ij} \right), \quad (3)$$

where $r_{ij} = P_j - P_i$. The resulting forces decay with distance to the fourth power, which is more rapidly than the field (and torque). The forces between dipoles are equal and opposite. Note that the relation between force and the agent acting as the field source (either m_i or m_j) is nonlinear (Abbott et al. 2020).

2.3 3D forward kinematics of two magnetic agents and magnetic inter-agent forces

Assumption field alignment. *The main assumption behind this work is that all magnetic moments on the mobile microrobot agents are all simultaneously aligned with the applied field.*

Throughout this paper, all distance variables are normalized by the agent size $2R$ which denotes the body diameter of agents if modeled as a sphere. These normalized distances are denoted by an asterisk. The system kinematics parameters are shown in Fig. 2. In local spherical coordinate frame $(\hat{e}_r, \hat{e}_\phi, \hat{e}_\theta)$ defined with respect to the pairwise separation vector with origin set at the position of the second agent, the radial, azimuth, and polar components of the local magnetic force exerted on the second agent by the first agent can be written as

$$f_r = \frac{\Omega}{r^4} [1 - 3 \cos^2(\alpha) \cos^2(\psi)], \quad (4a)$$

$$f_\phi = \frac{\Omega}{r^4} [\cos^2(\alpha) \sin(2\psi)], \text{ and} \quad (4b)$$

$$f_\theta = \frac{\Omega}{r^4} [\sin(2\alpha) \cos(\psi)]. \quad (4c)$$

The three orthogonal inter-agent force components are sketched as a function of local control input angles ψ and α in Fig. 3(A) to (C). Here $\Omega := \frac{3\mu_0 m_1 m_2}{4\pi}$ is the force constant. Permeability of free space is denoted by μ_0 , ψ is the local in-plane (yaw) control input angle defined as the angle between the projection of the applied field b_a in $(\hat{e}_r, \hat{e}_\phi)$ plane and the separation vector r . The out-of-plane (pitch) control input angle is denoted by α measured upward from $(\hat{e}_r, \hat{e}_\phi)$ plane. In 3D space, it is required to levitate the agents against their own weight by a constant force. This force needs to be strong unless we make agents neutrally buoyant.

2.4 Magnetic field strength requirement

The total field at the location of an agent is the vector sum of the inter-agent local field b_{21} (field on agent 2 created by agent 1) and the applied field b_a . To comply with the field

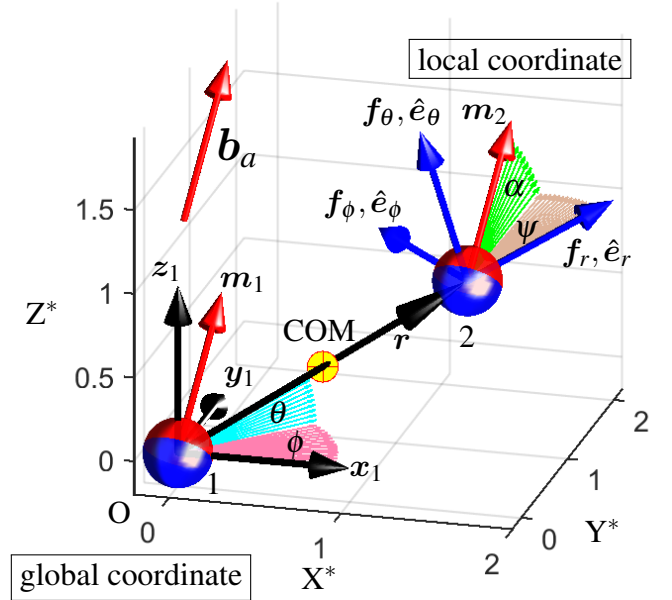


Fig. 2. 3D kinematics of two magnetic agents. The control inputs are angles yaw and pitch denoted by ψ and α , respectively, which characterize the heading of the applied field b_a in local coordinate with respect to the separation vector r . Local states of the system are $\bar{x}_{\text{local}} = [r \ \phi \ \theta]^\top$ describing the separation vector (local frames are shown in blue). These states are associated to the radial, azimuth, and polar inter-agent magnetic forces denoted by f_r , f_ϕ , and f_θ , respectively. The aforementioned three force vectors represent the local independently-controllable DOFs of the robot. Global states of the system are $\bar{x}_{\text{COM}} = [x_c \ y_c \ z_c]^\top$ associated to the center-of-mass (COM) of the team expressed in O_{XYZ} frame.

alignment assumption 2.3, b_a is required to dominate b_{21} . Here we check our assumption that the local field created by a nearby agent does not rotate the total field at an agent's location. In this respect, the applied field strength can be chosen such that the total field angle error less than a threshold given by $\theta_\epsilon = \gamma_a - \gamma$, where γ_a and γ respectively represent the actual and desired direct angles made between the total field and applied field with the radial coordinate r . One can express the desired angle γ as a function of in-plane ψ and out-of-plane α angles with $\gamma = \cos^{-1} \left[\frac{\cos(\alpha)(1 + \cos(2\psi))}{2 \cos(\psi)} \right]$. Also, the actual angle associated to the total field can be calculated as $\gamma_a = \angle b_{\text{tot}} = \angle (b_a + b_{12})$. For a given angle error threshold θ_ϵ , the minimum required field strength b_{\min} in this case is

$$b_{\min} = \frac{b - \sqrt{b^2 - 4ac}}{2a}. \quad (5)$$

Where

$$a = \frac{1}{A_1^2} - \frac{1}{A_2^2}, \quad (6a)$$

$$b = \frac{\mu_0 m \left(\frac{4}{A_1^2} + \frac{2}{A_2^2} - 3 \right)}{4\pi r^3}, \quad (6b)$$

$$c = \frac{-\mu_0^2 m^2 \left(\frac{-4}{A_1^2} + \frac{1}{A_2^2} + 6 \right)}{16\pi^2 r^6}, \quad (6c)$$

$$\text{where } A_1 = \cos(\theta_\epsilon + \cos^{-1}(A_2)), \text{ and } A_2 = \cos(\psi) \cos(\alpha).$$

Fig. 4 illustrates the minimum required field strength as a

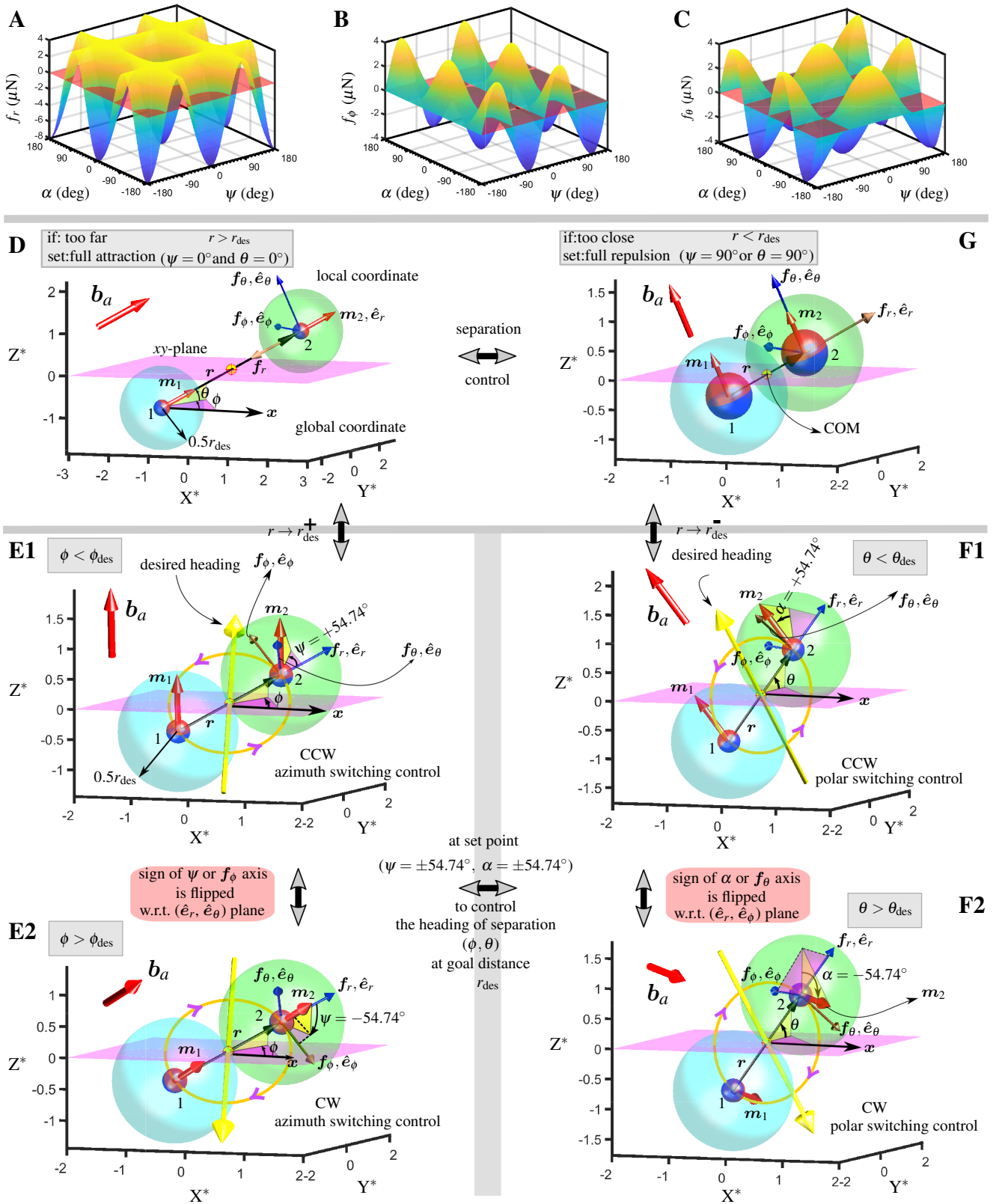


Fig. 3. The periodic instantaneous radial, azimuth, and polar force components of the inter-agent force are respectively graphed in (A), (B), and (C) as a function of two local control input angles ψ and α . The control inputs are the yaw and pitch angles denoted by ψ and α , respectively, which describes the heading of applied field b_a as well as the heading of m_1 and m_2 . Basic magnetic inter-agent control principle (Bang-Bang) of a pair of magnetic agents is sketched in spherical coordinate from reversible D to G cycle). The main assumption is that all magnetic moments are all aligned with applied field simultaneously. In each plot the active local force component is colored in brown to distinguish which force is responsible for the corresponding motion primitive. D) When two agents are too far put ($\psi = 0^\circ$ and $\alpha = 0^\circ$) to achieve full attraction f_r in the radial direction. When the separation between two agents reaches the desired distance (r_{des}), decision is made based on the sign of yaw or pitch angles associated to the applied field to regulate the heading of separation vector in either azimuth or polar directions sketched (from E1 to F2) via either azimuth f_ϕ or polar f_θ forces, respectively. G) When two agents are too close put ($\psi = 90^\circ$ or $\alpha = 90^\circ$) to achieve full repulsion f_r in the radial direction. Animation is available in the supplementary video.

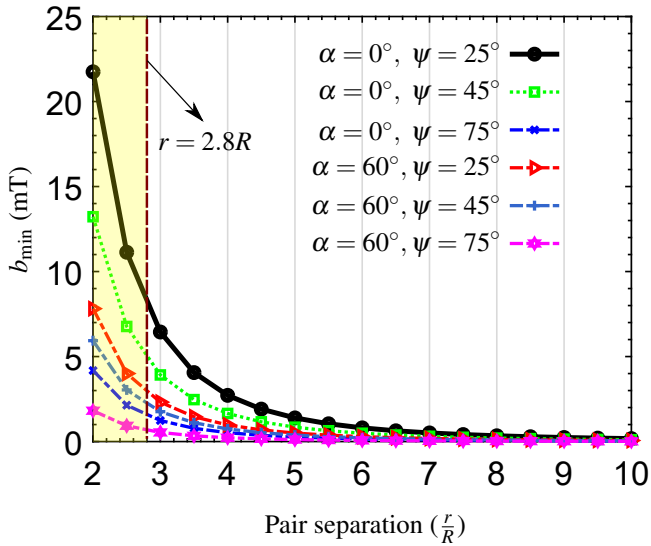


Fig. 4. Minimum required input field strength as a function of pair separation r for multiple control angles α and ψ to limit the total angle error to $\theta_e = 5^\circ$ ($|M| = 10^4$ A/m). The radius and magnetization of agents are denoted by R and M .

function of pair separation r for multiple control angle inputs ψ and α , using a maximum angle error of $\theta_e = 5^\circ$. For the experimental section of this paper, we maintain a field strength of 10 mT, to be higher than the minimum required field and assume that the agents always align with b_a . To control over separations shorter than $2.8R$, the minimum required input field strength needs to be increased significantly.

3 3D Position Control of Two-Agent Configuration

This section presents the control principle based on magnetic inter-agent forces that we developed to perform independent 6-DOF position control of two magnetic microrobots using a tri-axial Helmholtz coil system. The tri-axial Helmholtz coil system has six independent coils. As illustrated in Fig. 3, the relative positions of agents is simply set up by modulating the magnetization direction of agents through the change in the orientation of applied uniform magnetic field. The global position is controlled by pulling the center-of-mass (COM) of the team P_c through the generation of a magnetic field gradient superimposed over the uniform applied field.

3.1 Inter-agent control

Fig. 3(D) to (G) illustrates our inter-agent control principle to adjust internal states $\bar{x}_{\text{local}} = [r \ \phi \ \theta]^\top$ expressed in local spherical coordinate frame $O_{1x_1y_1z_1}$ (see Fig. 2) with respect to the separation vector. The pseudocode used to implement this localized controller is presented in Algorithm 1. The dynamic equilibrium of the underlying multi-agent system happens when two agents arrive at desired separation and pair heading orientation.

Importantly, as graphed in Fig. 3(A) to (C) at periodic setpoint angles, $\psi_s = 54.74^\circ$ and $\alpha_s = 54.74^\circ$, the radial force becomes zero (des stands for desired). If the 3D space between two agents is around the goal spacing ($r \approx r_{\text{des}}$),

Algorithm 1 Inter-agent force P-control algorithm

```

1: Local control inputs to system:  $\bar{u} = [\psi \ \alpha]^\top$ 
2: System outputs:  $\bar{x} = [r \ \phi \ \theta]^\top$ 

3: if  $r > r_{\text{des}}$  see Fig. 3(D) when agents are too far then
4:    $\psi \leftarrow 0$  and  $\alpha \leftarrow 0$ 
5: else if  $r < r_{\text{des}}$  see Fig. 3(G) when agents are too close then
6:    $\psi \leftarrow 90$  or  $\alpha \leftarrow 90$ 
7: else if  $r \approx r_{\text{des}}$  see Fig. 3(E1) to (F2) when agents get near goal separation then
8:   Synthesize P-controller
9:    $\psi \leftarrow \psi_s + k_{lp}(r - r_{\text{des}})$ , where  $k_{lp} > 0$  and  $\psi_s = \pm 54.74^\circ$ 
10:   $\alpha \leftarrow \alpha_s + k_{lp}(r - r_{\text{des}})$ , where  $\alpha_s = \pm 54.74^\circ$ 
11:  if  $\phi < \phi_{\text{des}}$  see Fig. 3(E1) then
12:     $\psi \leftarrow \psi$ 
13:  else if  $\phi > \phi_{\text{des}}$  see Fig. 3(E2) then
14:     $\psi \leftarrow -\psi$ 
15:  end if
16:  if  $\theta < \theta_{\text{des}}$  see Fig. 3(F1) then
17:     $\alpha \leftarrow \alpha$ 
18:  else if  $\theta > \theta_{\text{des}}$  see Fig. 3(F2) then
19:     $\alpha \leftarrow -\alpha$ 
20:  end if
21: end if

```

the controller would choose intermediate angles ψ and α locally between 0° and 90° centered around the setpoint, leading to the P-control law: $\psi \leftarrow \psi_s + k_{lp}(r - r_{\text{des}})$ and $\alpha \leftarrow \alpha_s + k_{lp}(r - r_{\text{des}})$ where k_{lp} represents the control gain, see Fig. 3(E) and (F) subplots. It can be seen from Fig. 3(A) to (C) that at any angle between 0 and 90° , a non-zero tangential force (f_ϕ or f_θ) occurs which causes the pair of microrobots to rotate about one another. By reflecting the control angle about $\psi = 0^\circ$ or $\alpha = 0^\circ$, the tangential forces can be reversed without affecting the radial force. This sign flipping enables the control of the pair heading's yaw ϕ or pitch θ angles around their goals ϕ_{des} or θ_{des} by constantly switching the rotation direction of the pair complex as shown in the state transition of Fig. 3(E) to (F). Readers are referred to Appendix A for stability proof of the local state controller at set point.

3.2 Team center-of-mass magnetic pulling in 3D

The center-of-mass of the team of agents represents global state of the system denoted by $\bar{x}_{\text{COM}} = P_c = [x_c \ y_c \ z_c]^\top$ and shown in Fig. 2. This state is controlled globally by external magnetic pulling. The uniform component of the field needs to be always kept on and remains at a constant magnitude (10 mT), whereas the field gradient can be varied as needed (up to a limit) so that it does not compromise the uniform field assumption 2.3. The gradient field could be turned off anytime to stop pulling the COM of the system. Animation is available in the supplementary video. In turn the velocity of each agent will be a net contribution of four motion primitives

that can be written for agent i as follows:

$$v_i = \frac{d\bar{x}_i}{dt} = \frac{1}{6\pi\mu R} \left[\underbrace{f_{r_i}\hat{e}_r + f_{\phi_i}\hat{e}_\phi + f_{\theta_i}\hat{e}_\theta}_{\text{inter-agent forces}} + \underbrace{f_P \frac{\mathbf{P}_{c_{des}} - \mathbf{P}_c}{\|\mathbf{P}_{c_{des}} - \mathbf{P}_c\|}}_{\text{COM pulling force}} \right]. \quad (7)$$

Three of these motion primitives refer to the projections of the inter-agent force in the radial, azimuth, and polar directions associated with the separation vector and denoted by f_{r_i} , f_{ϕ_i} , f_{θ_i} . The fourth motion primitive refers to the magnetic pulling f_P which is externally supplied by the magnetic generator system and attempts to pull agents from their current (\mathbf{P}_c) to desired center-of-mass ($\mathbf{P}_{c_{des}}$). The next section explains how to combine relationships 3.1 and 3.2 to construct the overall actuation matrix under the existing constraints and convert the four discussed primitives into desired system motion.

3.3 Combined field and force control

Typically in (1) the spatial derivative of the field (\mathbb{B}_∇) is considered as the system input to be controlled in the generation of pulling force f_P , and not \mathbf{m} . In fact the field-derivative matrix limits the number of truly independent quantities in any magnetic field (Abbott et al. 2020). As such (1) can be nonuniquely reformulated to separate the role of the manipulated dipole matrix \mathbb{M}_G from five independent spatial derivatives (“gradients” vector G). The elements of G are drawn from the elements of the field-derivative matrix \mathbb{B}_∇ in (1) as follows,

$$f_P = \mathbb{M}_G \{\mathbf{m}\} G, \quad (8)$$

$$\text{where } \mathbb{M}_G = \begin{bmatrix} m_x & m_y & m_z & 0 & 0 \\ 0 & m_x & 0 & m_y & m_z \\ -m_z & 0 & m_x & -m_z & m_y \end{bmatrix},$$

$$\text{and } G = \left[\frac{\partial b_x}{\partial x} \quad \frac{\partial b_x}{\partial y} \quad \frac{\partial b_x}{\partial z} \quad \frac{\partial b_y}{\partial y} \quad \frac{\partial b_y}{\partial z} \right]^\top.$$

The following discussion is valid for an array of n electromagnetic coil currents. However, we put our focus here on a tri-axial Helmholtz coil system which includes six orthogonal coils. The electromagnetic coil currents for a tri-axial Helmholtz coil system are given by,

$$\mathbf{I} = [I_{x^-} \ I_{x^+} \ I_{y^-} \ I_{y^+} \ I_{z^-} \ I_{z^+}]^\top. \quad (9)$$

The following equation maps the array of n electromagnetic coil currents \mathbf{I} to the output vector \mathbf{Y} enclosing magnetic field and global pulling force at workspace through the “actuation” matrix \mathbb{S} .

$$\mathbf{Y} = \begin{bmatrix} \mathbf{b} \\ \mathbf{f}_P \end{bmatrix} = [b_x \ b_y \ b_z \ f_{P_x} \ f_{P_y} \ f_{P_z}]^\top = \mathbb{S}_{6 \times n} \mathbf{I}_{n \times 1}, \quad (10)$$

such that,

$$\mathbb{S} = \mathbb{M}_{\mathbf{b}, \mathbf{f}_P} \mathbb{F}_{8 \times n}, \quad (11)$$

with the “coil” matrix $\mathbb{F} = [\mathbb{B}^\top \ \mathbb{G}^\top]^\top$ which is partitioned into its field \mathbb{B} and field-gradient \mathbb{G} matrix components and has the role to map the vector of six coil currents \mathbf{I} to the

vector of eight desired magnetic field inputs $\mathbf{U} = [\mathbf{b}^\top \ \mathbf{G}^\top]^\top$ via $\mathbf{U} = \mathbb{F} \mathbf{I}$. Also, the “system’s manipulation” matrix maps the magnetic field input vector \mathbf{U} to the pulling force vector f_P , and is expressed as,

$$\mathbb{M}_{\mathbf{b}, \mathbf{f}_P} \{\mathbf{m}\} = \begin{bmatrix} \mathbb{I}_3 & \mathbf{0}_{3 \times 5} \\ \mathbf{0}_{3 \times 3} & \mathbb{M}_G \{\mathbf{m}\} \end{bmatrix}. \quad (12)$$

Each column of the \mathbb{F} matrix corresponds to one of the field generating coils. One can either obtain each element of \mathbb{F} matrix fully throughout experimental calibration or in our case based on the Biot-Savart law and matrix transformations. In this respect, we obtained the unit current-field map after explicitly measuring the magnetic field at the center of our tri-axial Helmholtz coil system, and then analytically computed the gradients of field components with calibration based on the involved geometrical parameters (see equations (15-18) in (Salmanipour and Diller 2018) for more information). Following the standard setup notations introduced above, the coil matrix representing our tri-axial Helmholtz coil generator is derived as

$$\mathbb{F} = \begin{bmatrix} 3.6 & 3.6 & 0 & 0 & 0 & 0 \\ 0 & 0 & 3.5 & 3.5 & 0 & 0 \\ 0 & 0 & 0 & 0 & 3.5 & 3.5 \\ \hline -40 & 40 & 40 & -40 & 30 & -30 \\ 0 & 0 & 0 & 0 & 0 & 0 \\ 0 & 0 & 0 & 0 & 0 & 0 \\ 20 & -20 & -90 & 90 & 30 & -30 \\ 0 & 0 & 0 & 0 & 0 & 0 \end{bmatrix}. \quad (13)$$

The field associated entries above the line in matrix \mathbb{F} have [mT] unit, and the field gradient associated entries below the line have [mT/m] unit. Calculating the rank of matrix $\mathbb{G}\mathbb{N}_\mathbb{B}$ (see (11)) for a tri-axial Helmholtz coil system, where $\mathbb{N}_\mathbb{B} \equiv \left(\mathbb{I}_n - \mathbb{B}^\top \left(\mathbb{B}\mathbb{B}^\top \right)^\dagger \mathbb{B} \right)$ is the right null space of \mathbb{B} , quantifies the number of field-derivatives that the system is capable to control independently from the field, which is only 2 in normal scenario for this type of coil system as supposed to 5 for an OctoMag system (Petruska and Nelson 2015). Note that the actuation matrix for a tri-axial Helmholtz coil system is assumed invariant to the position of agents moving near the center of workspace due to the system’s capability to generate uniform field and gradient.

3.4 Pseudoinverse current solution

Petruska and Nelson (Petruska and Nelson 2015) showed that the minimum number of coils needed to create any desired force direction on a single agent at any requested input of uniform field is eight. Apparently compared with a tri-axial Helmholtz coil system an 8-coil system such as Octomag is expected to yield a better result as it does not attribute to any singularities in the generation of a field gradient in desired direction. But we decided to use tri-axial Helmholtz coil system because of two reasons: 1) Having applied our method to a Helmholtz coil system considered as a relatively harder case than an 8-coil system, we aimed to demonstrate that our control principle solution can be easily generalized in a similar routine, to any other type of magnetic generator system. 2) The available uniform field workspace produced by

our existing Octomag system in our lab was not adequate to span the uniform field volume required by our team of agents.

The tri-axial Helmholtz coil system is capable to generate uniform-gradient fields (Yesin et al. 2006) but owns a rank-deficient actuation matrix. As a result, 3D pulling along a straight path connecting team's center-of-mass to goal may not be exactly achievable. However, one can still decompose the straight path into feasible paths for which force would exist. For a desired field/force vector, the optimal solution of coil currents that gets us closest to the desired torque/force value can be found using the pseudoinverse of the actuation matrix S_Y , which returns the value that minimizes $\|I\|$ subject to the constraint that the norm of output vector error $\|S_Y I - [b_{des} \ f_{P_{des}}]^T\|$ is minimized. Due to the constraint on the uniform field both in direction and magnitude assigned identically to all agents, b_{des} should be pre-conditioned over $f_{P_{des}}$. Algorithm 2 renders how to synthesize the coil currents to accomplish desired combined field and pulling force so that the spacing and center-of-mass of the team of agents can be regulated.

Algorithm 2 Synthesis of coil currents algorithm

- 1: **Global control input to system:** $f_{P_{des}}$ and b_{des}
 - 2: **System output:** The vector of coil currents I
 - 3: Construct the pulling action $f_{P_{des}} = k_P(P_{c_{des}} - P_c)$
 - 4: Construct the applied field b_{des} with control inputs ψ and α obtained from Algorithm 1
 - 5: Calculate the coil currents I from pseudoinverse current solver: $I = S_Y^\dagger [b_{des} \ f_{P_{des}}]^T$ by taking $f_{P_{des}}$ as input from step 3 subject to the constraint on b_{des} made in step 4. Choose the one that minimizes $\|I\|$ in case of multiple current solutions.
-

A singularity refers to a direction along which a desired exact force cannot be generated.

Remark 1. *The following two points are considered in our pulling actuation design:*

- *The worst-case force singularity occurs when $|\angle f_{P_{des}} - \angle f_P| > 90^\circ$ or equivalently $\|f_{P_{des}} - f_P\|$ exceeds a certain threshold. Whenever this condition occurs the pulling action is turned off.*
- *In case generating a desired pulling force demands larger than a certain threshold power, we normalize the current proportionally to make sure at least the direction of pulling force would be correct.*

To perform field and force control, we consider the combined matrix S known as actuation matrix in (11). Here we study the reachable force space that can be generated via a tri-axial Helmholtz coil system. We show that this space is limited and at each instant of actuation time there is always a dipole-moment direction at which the achievable forces decrease from a 3D-space to a 2D-space.

3.5 Is the center-of-mass external magnetic pulling of the multi-agent system possible in 3D using an underactuated magnetic field generator?

Here we analyze the singularity for a six mutually orthogonal and independent electromagnets based on Helmholtz configuration, but can extend the same idea to any other magnetic setup developed for a multi-agent system. At singular configurations, S loses rank compromising the system independent actuation. These singularities are due to the nonexistence of the current to explicitly generate a desired force constrained by the field's orientation and magnitude as well as coil configuration.

3.5.1 Quantifying accuracy cloud of the pulling force Here we quantify how varying the control input (magnetization or equivalently applied uniform field) in global coordinates affects the pulling capability at the COM of the team. Let \mathbb{A} map out the current to the pulling force written as $f_P = \mathbb{A}I$. The nature of existing singularities becomes evident after applying the singular value decomposition (SVD) to decompose \mathbb{A} as

$$\mathbb{A} = U\Sigma V^T, \quad (14)$$

where the input current singular vectors are the columns of the orthonormal $V = [v_1, \dots, v_n]$, the output force singular vectors are the columns of the orthonormal $U = [u_1, \dots, u_n]$, and the singular value matrix Σ is of the form

$$\Sigma = \begin{bmatrix} \sigma_1 & 0 & 0 & 0 & 0 \\ 0 & \sigma_2 & 0 & 0 & \dots & 0 \\ 0 & 0 & \sigma_3 & 0 & 0 & 0 \end{bmatrix}_{3 \times 6}. \quad (15)$$

We need this tool because \mathbb{A} is non-invertible in our case and will allow us to identify the accuracy cloud or maximum likelihood of pulling force distribution in 3D for the multi-agent system. For full 3-DOF pulling force control, all the three singular values must be nonzero. In Fig. 5, the singular values, σ_1 through σ_3 , describe the relative strength of the pulling force in the three orthogonal directions of the output force singular vectors (U-basis), which do not necessarily correspond to the principal axes of the workspace (E-basis) or the separation vector. E in E-basis stands for the world frame's Euclidean space. Fig. 5(A) to (C) confirm that for a virtual single agent centered at the origin singularity appears (red arrow) if the magnetization is kept stationary. Hence, the force space will be a plane. However, remarkably, since the magnetization input constantly varies by the local control input angles ψ and α at the subsequent short period of times around a "central" magnetization axis, e.g. $\bar{m}_{(110)}$ in Fig 5(D), the reachable force space will span a 3D cloud. This unique switching property of our control law not only enables regulation of the team's orientation, but also makes the 3D pulling possible using a tri-axial Helmholtz coil system with a rank-deficient actuation matrix.

Lemma 1. *Consider that Assumption 2.3 holds and direction of separation vector and agents' magnetization continuously modulates in the global workspace frame at all times $\forall t \in \mathbb{R}$. Then, the time-averaged pulling force spaces will span a filled elliptical volume for a tri-axial Helmholtz coil.*

$$\langle \mathbf{f}_{P_1}, \mathbf{f}_{P_2} \rangle = [\mathbb{A}_1 | \mathbb{A}_2] \begin{bmatrix} \mathbf{I}_1 \\ \mathbf{I}_2 \end{bmatrix} = \underbrace{\begin{bmatrix} 0 & 0 & 0 & m_{t_1x} & \vdots & \vdots & 0 & \vdots \\ 0 & 0 & 0 & 0 & \vdots & \vdots & m_{t_1y} & \vdots \\ 0 & 0 & 0 & -m_{t_1z} & \vdots & \vdots & -m_{t_1z} & \vdots \end{bmatrix}}_{\mathcal{C}_1(\mathbf{m}_1)} \underbrace{\begin{bmatrix} 0 & 0 & 0 & m_{t_2x} & \vdots & \vdots & 0 & \vdots \\ 0 & 0 & 0 & 0 & \vdots & \vdots & m_{t_2y} & \vdots \\ 0 & 0 & 0 & -m_{t_2z} & \vdots & \vdots & -m_{t_2z} & \vdots \end{bmatrix}}_{\mathcal{C}_2(\mathbf{m}_2)} \begin{bmatrix} \mathbb{F}_{8 \times 6} & | & \mathbf{0} \\ \mathbf{0} & | & \mathbb{F}_{8 \times 6} \end{bmatrix} \begin{bmatrix} \mathbf{I}_1 \\ \mathbf{I}_2 \end{bmatrix}. \quad (16)$$

Proof. Let $\mathbf{f}_{P_1} = \mathbb{A}_1 \mathbf{I}_1$ and $\mathbf{f}_{P_2} = \mathbb{A}_2 \mathbf{I}_2$ represent the force vector spaces occur at two successive times t_1 and $t_1 + \Delta t$ such that $\Delta t \rightarrow 0$, subject to two non-collinear magnetization inputs \mathbf{m}_{t_1} and \mathbf{m}_{t_2} respectively, then based on (11) the time-averaged force can be written as equation (16) above. Here we prove why the resulting matrix $[\mathbb{A}_1 | \mathbb{A}_2]$ which is the horizontal concatenation of two actuation matrices at two successive times will get full rank. Without loss of generality, the representative matrix \mathbb{F} in equation (13) voids all columns in each of matrices \mathcal{C}_1 and \mathcal{C}_2 in (16) except their 4th and 7th columns as highlighted. Given that m_{t_1x} , m_{t_1y} , and m_{t_1z} appear at mutually orthogonal row entries in \mathcal{C}_1 , it can be concluded that there are no worse *central* magnetizations other than those aligned with the coil's principal axes at which the column rank of \mathbf{f}_{P_1} would reduce to one as the lowest rank possible at t_1 . To construct \mathbf{f}_{P_2} at subsequent time slot $t_1 + \Delta t$ let ε_1 and ε_2 represent the nonzero continuous deviations of \mathbf{m}_{t_2} away from the worst case *central* magnetization \mathbf{m}_{t_1} by local control input angles ψ and α , then the absolute determinant of the augmented manipulation matrix \mathbb{C} is calculated as $\text{abs}(|\mathbb{C}|) = \varepsilon_1 \varepsilon_2 \neq 0$ where $\mathbb{C} = [\mathcal{C}_1(\mathbf{m}_{t_1}) | \mathcal{C}_2(\mathbf{m}_{t_2})]$. Thus, matrix \mathbb{C} gets full rank. Since $\text{rank}(\mathbb{F}) = 5$ for a tri-axial Helmholtz coil system, therefore, the total actuation matrix $[\mathbb{A}_1 | \mathbb{A}_2]$ will get full row rank. For example, for the principal magnetization $\mathbf{m}_{t_1} = [1 \ 0 \ 0]^T$ only three orthogonal columns in \mathbb{C} will stay intact (the zero columns are removed) rendered as,

$$\text{row rank}(\mathbb{C}) = \text{rank} \begin{bmatrix} 1 & 1 & 0 \\ 0 & 0 & \varepsilon_1 \\ 0 & -\varepsilon_2 & -\varepsilon_2 \end{bmatrix} = 3 \quad (17)$$

Consequently, two force spaces \mathbf{f}_{P_1} and \mathbf{f}_{P_2} will merge and the intersection of Nullspaces would change from plane (2D) or line (1D) to point (0D). Hence, on average it makes it possible to move agents asymptotically toward pulling goal. ■

3.5.2 Correlation between the separation and force distribution Our simulations show that under the imposed constraint that agents' magnetization has to continuously sweep around the separation vector to maintain the agents pair at desired pair heading, then the external pulling force on each agent will fill an elliptical volume as computed and illustrated in Fig. 5 (E-F). Here we report on the optimal and weakest scenarios that exist in pulling capability as the separation vector varies. We can use a performance index κ to evaluate the relative strength of the force that can be generated in different directions:

$$\kappa = \frac{\sigma_r}{\sigma_l}. \quad (18)$$

To some applications of interest, one may need to treat a pair of agents as a dynamic entity and determine a direction along which a pair of agents can exert maximum force to

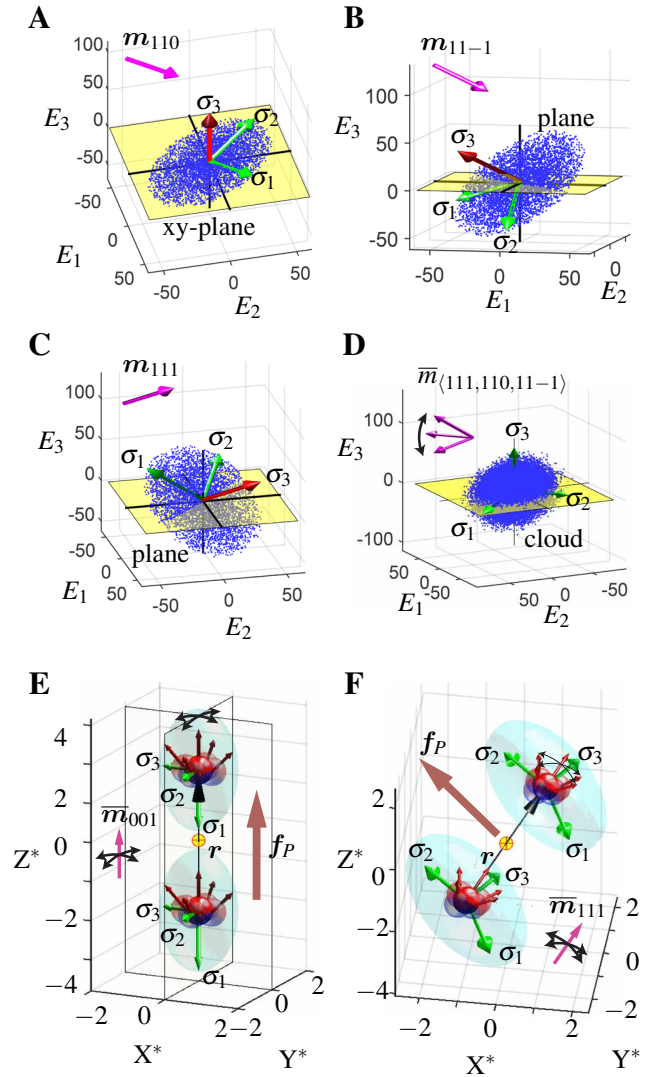


Fig. 5. Quantification of the magnetic pulling force distribution on a pair of agents for a given unit-strength dipole moment's input. From (A) to (D) the accuracy cloud of the magnetic pulling force exerted on a virtual single agent centered at the origin is represented in the world frame's E -basis with U -basis in green/red (red shows singular direction). Analyses are performed for different magnetizations: (A) $\mathbf{m} = [1 \ 1 \ 0]^T$, (B) $\mathbf{m} = [1 \ 1 \ -1]^T$, (C) $\mathbf{m} = [1 \ 1 \ 1]^T$, and (D) time-averaged magnetization $\bar{\mathbf{m}} = \langle 111, 110, 11 - 1 \rangle$. As extended examples for the pair of agents, the composed elliptical pulling force accuracy cloud is sketched around each agent in (E) for time-varying magnetization input $\bar{\mathbf{m}}_{(001)}$, and in (F) for time-varying magnetization input $\bar{\mathbf{m}}_{(111)}$, while local controller modulates magnetization temporally around the given central magnetization in $\langle \cdot \rangle$ by ψ and α to maintain two agents at desired separation's heading. Alternatively, the COM of system can be used to describe the system's drag response to external magnetic pulling force. The brown \mathbf{f}_P vector shows the major direction of the pulling force distribution that can be achieved for the desired separation heading.

manipulate a cargo. To this end, we introduce κ to compare the pulling force component along the separation vector σ_r to the major orthogonal force basis σ_1 , approximated using standard equation of an ellipse where,

$$\sigma_r = \frac{\sigma_1 \sigma_3}{\sigma_3^2 |\sin(a) \sin(b)| + \sigma_1^2 |\cos(a) \cos(b)|} \text{ with}$$

$$a = 2(\phi - \frac{\pi}{4}) \text{ and } b = 2(\theta - \frac{\pi}{4}). \quad (19)$$

Here, σ_3 represents the minor orthogonal force basis. For instance, $\kappa = 1$ indicates that the strongest force would occur along the separation vector when separation vector can align with principle axes of the workspace frame shown in Fig. 5(E) as one example. In other words, the force cloud elongates along the separation vector. Lowest κ configuration occurs when separation vector needs to align with workspace diagonal axis displayed in Fig. 5(F). Namely, the force cloud elongates perpendicular to the separation vector. Conventionally, a different way to define κ is through force condition number $\frac{\sigma_3}{\sigma_1}$ (Kummer et al. 2010), which in the context of this paper describes how isotropic the pulling force distribution globally will be as the magnetization changes.

3.6 Generic solution to more agents: Optimization-based control (OBC)

Two-agent configuration is a building block of a team of microrobots. This part presents a structural compact solution that generalizes the inter-agent force P-control algorithm (1) for more agents configured at a prespecified geometry.

Let ${}^i \mathbf{f}_{\text{tot}}$ denote the total force vector created at the location of agent i by the rest of agents of the set, then ${}^i \mathbf{f}_{\text{tot}} = \sum_{k \neq i} \mathbf{f}_{ki}$ whereby $k \in \{1, 2, \dots, n\}$ with n as the number of agents, and \mathbf{f}_{ki} is the pairwise magnetic force exerted at the location of agent i solely by agent k , calculated by (3). In local spherical coordinates defined exclusively for each pair of agents ($\hat{e}_{r_{ij}}, \hat{e}_{\phi_{ij}}, \hat{e}_{\theta_{ij}}$), the net radial, azimuth, and polar components of the total magnetic inter-agent forces linked to pair ij can be written as

$${}^{ij} f_r = ({}^i \mathbf{f}_{\text{tot}} - {}^j \mathbf{f}_{\text{tot}}) \cdot \hat{e}_{r_{ij}}, \quad (20a)$$

$${}^{ij} f_\phi = ({}^i \mathbf{f}_{\text{tot}} - {}^j \mathbf{f}_{\text{tot}}) \cdot \hat{e}_{\phi_{ij}}, \text{ and} \quad (20b)$$

$${}^{ij} f_\theta = ({}^i \mathbf{f}_{\text{tot}} - {}^j \mathbf{f}_{\text{tot}}) \cdot \hat{e}_{\theta_{ij}}. \quad (20c)$$

3.6.1 Fitness function The goal is to find ψ and α angles solution that minimizes a weighted L^2 -norm fitness function so that the relative spacings and angles of the pairs are pushed toward the desired ones between a set of n magnetic agents in 3D. Let's state our optimization problem as follows:

$$(\psi^*, \alpha^*) = \arg \min_{\psi, \alpha} \mathcal{F} = \sum_{i,j=1}^n |\varphi(\tilde{r}_{ij}[t+1|t]) + \gamma_r {}^{ij} f_r|^2$$

$$+ \lambda_\phi \sum_{i,j=1}^n |\varphi(\tilde{\phi}_{ij}[t+1|t]) + \gamma_\phi {}^{ij} f_\phi|^2 D(\frac{\tilde{\phi}_{ij}}{\Gamma_\phi})$$

$$+ \lambda_\theta \sum_{i,j=1}^n |\varphi(\tilde{\theta}_{ij}[t+1|t]) + \gamma_\theta {}^{ij} f_\theta|^2 D(\frac{\tilde{\theta}_{ij}}{\Gamma_\theta}). \quad (21)$$

The proposed fitness function is a weighted sum of *corrective* radial, azimuth, and polar forces. To distinguish the opposite sign of these forces that infers at each sampling time whether for the associated link r_{ij} the net radial force ${}^{ij} f_r$ obtained in (20) gets attractive or repulsive, or when each of the net azimuth ${}^{ij} f_\phi$ or polar ${}^{ij} f_\theta$ forces turns the pair of agents in clockwise (CW) or counter-clockwise (CCW) directions, navigation function $\varphi(\cdot)$ is considered. This navigation function could be either a binary function such as $\varphi = \text{sgn}(\cdot)$ leading to a binary response around the desired states, or a smooth logistic function such as $\varphi(\tilde{x}) = 2(\frac{1}{1+e^{-\beta \tilde{x}}} - 0.5)$, wherein the conditional predictive error of each input state for the next sampling time under the current time (e.g. $\tilde{r}[t+1|t] = r - r_{\text{des}}$) is denoted by \tilde{x} and the slope of convergence along each state primitive directions toward the goal is denoted by β . The *corrective* forces are chosen to represent the definition of three modified forces by their navigation function.

It should be noted that the navigation function $\varphi(\cdot)$ consideration would have a high impact to save the computation time and provides a compact type solution for the generic multi-agent problem. Also λ denotes the weight to specify the tracking of whichever state of separation r or pair heading angles ϕ and θ is more important for a particular trajectory to be shaped. For any arbitrary pair taken within the multi-agent set, the error in azimuth and polar states ϕ and θ are denoted by $\tilde{\phi}_{ij}$ and $\tilde{\theta}_{ij}$, and get zero at $\psi = 0^\circ$ or 90° . However, these angles may spontaneously generate undesirable possible maximum radial force that would lead to a small steady error in separation state (for further details refer to (Salehizadeh and Diller 2017b)). One can simply compensate this small artifact by defining a dead-zone $D(\cdot)$ over the azimuth and polar angle states with a small width Γ around 0.5° . The proposed \mathcal{F} in (21) is a periodic scalar-valued bivariate quadratic fitness function. Given that our multi-agent problem is high dimensional with a nonconvex fitness function, a real-time informed gradient descent optimization solver is used for solving the nonlinear relationship between input field orientation and agents positions. To implement partial derivatives numerical finite difference approximation is used.

3.6.2 Multiple global minima As shown in Fig. 3(A) to (C), the inter-agent forces associated to a pair of agents are periodic by 360 degrees. Though since our fitness function in (21) utilizes the *corrective* force definition by taking into account the state error sign, that modification yields symmetry to the function; as such the period of the overall fitness function will reduce to 180 degrees. This periodic property of fitness function introduces multiple global minima solutions which of course are equivalent. Our experimental observations imply that rapid jumps between different global minima over the period of 360 degrees at different time steps has positive impact exceptionally for an underactuated tri-axial Helmholtz coil system since the system singularities in the pulling force generation can be improved by setting no bounds on the search domain of the control angles. On the other hand, as a trade-off, in practice agents have to magnetically reorient from past to current solution angles. Thus, they would physically have to sweep over intermediate range of angles which would potentially generate undesirable forces. Therefore, in case of

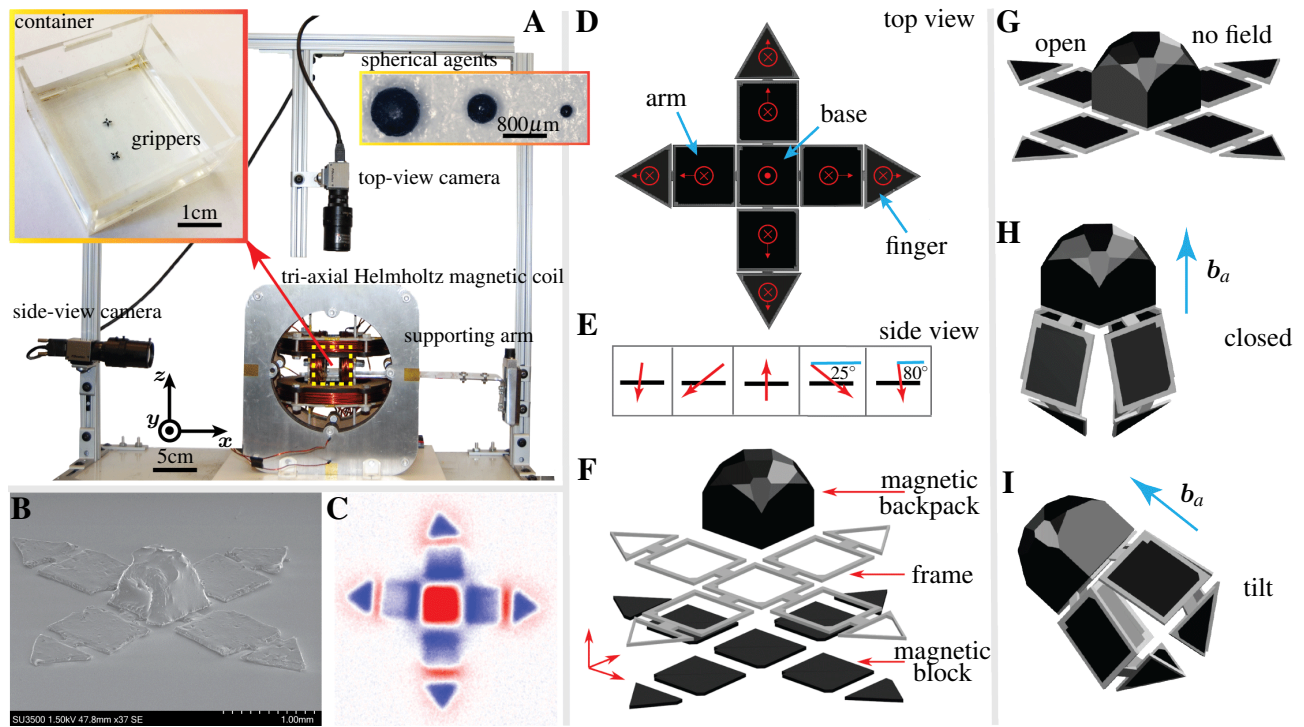


Fig. 6. Our experimental setup, structure and working principle of the microgripper is shown: (A) Two microgrippers are submerged in glycerol inside the container located in the middle of a tri-axial Helmholtz coil. The 3D position of two microrobots is read via top and side-view cameras. SEM and magneto-optical sensor image of the fully assembled microgripper are shown in (B) and (C), respectively. In (C) red and blue gradient colors imply the positive and negative magnetic field strengths along the z-axis, respectively. Magnetization profile of the microgripper from top and side views are illustrated in (D) and (E). Exploded drawing of microgripper is shown in (F). From (G) to (I) different manipulation states of a microgripper are displayed. When magnetic field is absent, the microgripper remains open, see (G). The microgripper closes once a magnetic field is applied along its central axis, see (H). And its orientation is always aligned with the direction of the applied magnetic field, see (I).

a fully actuated coil system such as OctoMag, to achieve an ideal performance and to reduce the jumps, it is recommended to wrap the optimal solution angles to the fundamental period of \mathcal{F} function at 180 degrees.

4 System implementation

This section introduces the experimental setup and fabrication methods to create spherical and gripper microrobots.

4.1 Experimental setup

Magnetic fields for agent actuation are created in an electromagnetic coil system with three pairs of coils nested orthogonally to create fields in 3D, powered by three pairs of analog servo drives (30A8, Advanced Motion Controls) and controlled via a DAQ I/O board (Model 826, Sensoray). Each pair of wire loops in the coil system is arranged in Helmholtz configuration, resulting in a uniform magnetic field up to 15 mT (uniform to within 5% of nominal at the center over a workspace cube with the side length of 5 cm) located at center of the coil system, see Fig. 6(A). Agents' positions are detected using two cameras (FO134TC, FOculus) mounted atop and aside the workspace, and a computer with custom C++ code finds each agent center position using a Hough-circle/bounding-rect transforms in the OpenCV library at 60 frames/second. To calibrate the camera a linear triangulation of the two views is performed.

4.2 Fabrication of agents

4.2.1 Spherical agents The fabrication process of our spherical agents which are illustrated in the right inset of Fig. 6(A) are explained in detail in (Salehizadeh and Diller 2017b) under section 4.2, except, we combine the main composite with hollow glass beads (3M Glass Bubbles K20) at a mass ratio of 10:1 to make the agents neutrally buoyant for the target fluid density. Owing to the high magnetic coercivity of (MQFP-15-7-20065, NdPrFeB, Magnequench) magnetic powders embedded in the magnetic agents (that is, $450 \frac{kA}{m}$), these microrobots were not subject to demagnetization from the relatively weak fields applied in this work.

4.2.2 Gripper agents We fabricated grippers to be utilized as functional microrobot samples in this work based on our previous papers (Zhang et al. 2018; Xu et al. 2019). The left inset of Fig. 6(A) displays a pair of these agents floating inside diluted glycerol solution. The SEM image of the gripper with its backpack is captured in Fig. 6(B). We validated the magnetic profile accuracy of the gripper by viewing the distribution of the magnetic flux at sample surfaces using a magneto-optical sensor (MagView S, Matesy GmbH) shown in Fig. 6(C). These microgrippers are composed of magnetic elastic polymers with embedded permanent magnetic microparticles and are identical to those used in (Zhang et al. 2018). Each microgripper is symmetric about its center with nine magnetic blocks, one magnetic backpack, and one nonmagnetic frame that links neighboring blocks together, see Fig. 6(D) to (F). To lighten grippers we used

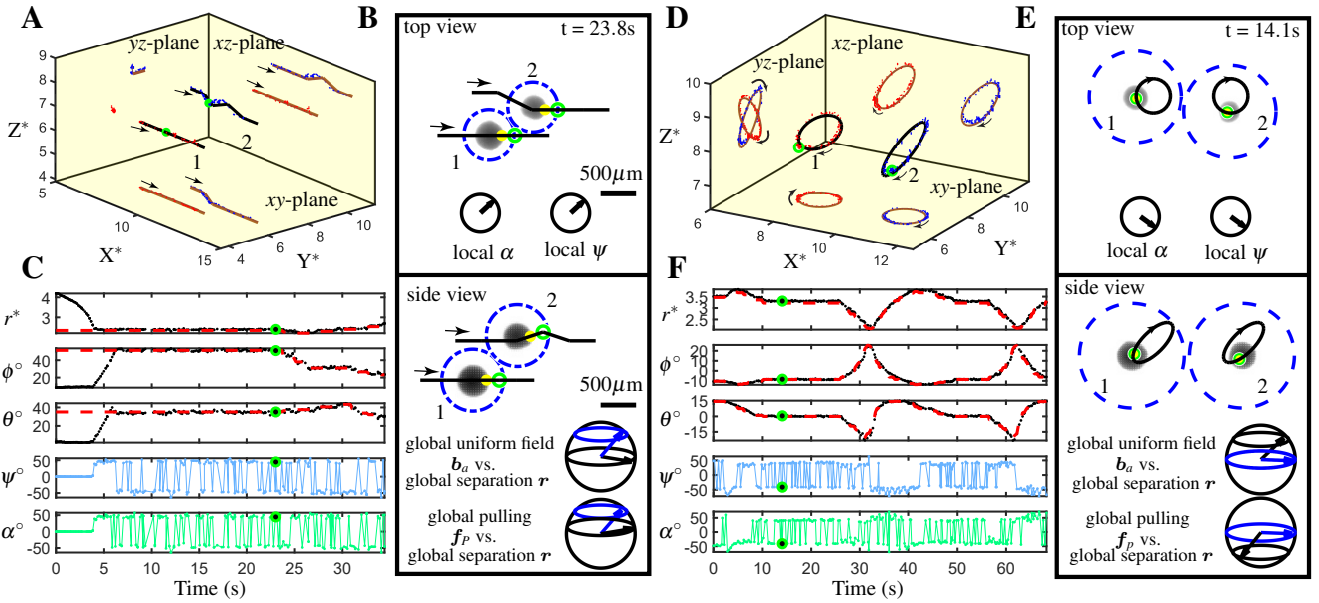


Fig. 7. Experimental results showing path following of two magnetic microspheres in 3D using independent position control for two examples: 1) line-shaped (A to C), and 2) ellipse-shaped formations (D to F). 3D position of two agents are sketched in (A) and (D). A Snapshot of top and side-view frames of the workspace are shown at a specific time in (B) and (E) (noted at top right corner and also marked by green circles in every subplots). The solid paths represents the desired paths. The dashed circle around each agent has radius equal to $0.5r_{des}$ and indicates when two agents arrive at desired separations. The yellow circle associates to the moving goal which is linearly constructed based on two subsequent original waypoint goals to ensure agents move straight toward goal as much as possible. The time response tracking of the local states $\bar{x}_{local} = [r \ \phi \ \theta]^T$ associated to the separation vector and local control inputs $\bar{u}_{local} = [\psi \ \alpha]^T$ are illustrated in (C) and (F). Here the desired tracking signals are shown in red dashed lines. Video is available in supplementary materials.

UV-cure glue to attach glass beads on top of backpack. The working principle of the microgripper is described in the caption of Fig. 6(G) to (I). The microgripper's backpack has a magnetic moment along the microgripper central axis. The backpack is used to increase the net magnetic moment of the whole microgripper, in order to enhance the magnetic interactions between two microgrippers within the workspace. Fabrication details can be found in our previous work (Zhang et al. 2018).

5 Experimental Results

This section provides our 3D experimental demonstrations implemented on a pair of spherical as well as functional magnetic microgripping microrobots.

5.1 Independent motion control of two magnetic microrobots

This section presents our path tracking result implemented on two magnetic spherical particle microrobots in 3D. Fig. 7 shows the functionality of our magnetic team control through the navigation of two magnetic spherical microrobots along two paths: 1) line-shaped formation, and 2) ellipse-shaped formation. The experimental 3D position of two magnetic agents are sketched in Fig. 7(A) and (D) for the two paths, while the path projections on top/side-view planes are displayed. To compensate the gravity impact, we integrated our P-controller with an integral action along the z -axis. A snapshot of top and side-view frames of the workspace are shown at a specific time in Fig. 7(B) and (E). The local control input signals ψ and α are given by arrow indicators

on top-view windows. Also the 3D global uniform applied field b_a and the pulling force f_p indicators are pictured with respect to the 3D separation vector r , where one can infer the behavior of system. The time response tracking of the local states and local control inputs are graphed in Fig. 7(C) and (F), which implies to a good agreement between the actual and desired signal tracking.

For hard magnets the inter-agent forces are independent of field strength assuming the alignment assumption is satisfied. For soft magnets, the magnetization of the agents will be field dependent, and so the inter-agent forces will be field magnitude squared dependent. As such for soft magnets the inter-agent forces can be weaker or stronger depending on the material and the applied field. However, regardless of soft or hard, as long as a strong input field with a constant magnitude applies, the inter-agent force control would work because then it would be only dependent on the orientation of the field.

The estimated controllable range of inter-agent separation is scalable based on the agents characteristic body radii R , obtained as $(2.8R < r < 10R)$ to keep agents mutually interactive through their field and avoid the occurrence of overpower phenomena as discussed in part 2.4. Despite the short range of pairwise separation possible, many cooperative micromanipulation tasks such as grasping, pushing, caging (Wang et al. 2018), microfluidic microfactory (Yu et al. 2020), multiple cell trapping into MEMS tool channels for parallel testing (Elhebeary and Saif 2017), assembly and disassembly rely on independent actuation within close proximity. The next section presents one of these applications performed by functional microrobots running parallel tasks, which is solved using inter-agent force

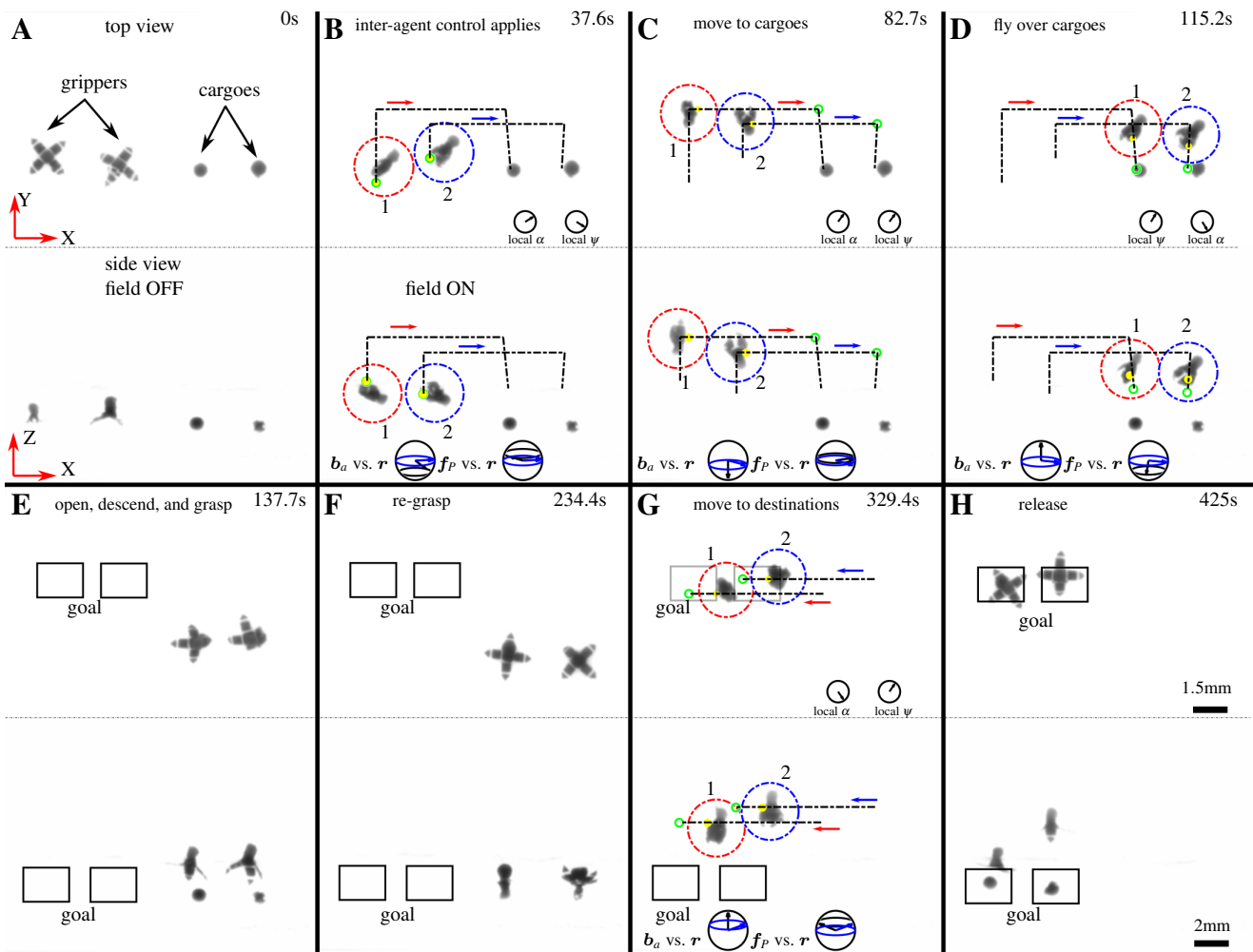


Fig. 8. Experimental setup and results of two microgrippers picking and placing two cargoes in 3D. Two microgrippers and two cargoes are submerged in Glycerol, which is monitored by two cameras from top and side views. A sequence of top and side-view frames of the workspace is shown chronologically from (A) to (H) with the actuation mechanism noted. The local and global control inputs indicators are provided with respect to the global pos of the separation vector at the bottom of each window. Video is available in supplementary materials.

control. In case actuation over larger separations would be desired which happens when agents get too far from each other, the proposed actuation can always be combined with other existing methods such as (Ongaro et al. 2019).

5.2 Demonstration: autonomous 3D cargo delivery using two magnetic microgrippers

This experiment demonstrates the efficacy of the proposed control scheme to independently and simultaneously position two microgrippers to pick-and-place two cargoes.

5.2.1 Gripper motivation

Here we chose microgrippers as just one example of functional microrobots which their special functional characteristics (i.e. gripping, or grasp and release manipulation mechanism) can be integrated with our inter-agent formation controller to do a complete cargo team delivery task. An unconstrained rigid magnetic microgripper has six free axes of which we can control three translational axes and the opening/closing angle using the proposed method. Thus, each individual gripper may have 4 actuated DOFs.

5.2.2 Grippers team actuation

An example on how our inter-agent control technique can be employed for a team of microgrippers to reliably perform cargo pick-and-place and transportation tasks is shown in Fig. 8. The control task can be classified into two layers as follows:

Upper layer — path planner The upper layer is responsible to process the feedback information and decides the next set of actions. The upper layer extracts and triangulates the 3D present positions of the microgrippers and cargoes from visual feedback, i.e., the real-time frames captured by top and side-view cameras, using a contour-finding algorithm from the OpenCV library. Then the path planner uses these positions to calculate the next desired positions for the two microgrippers. The path planner activates the formation controller in the lower layer if the microgrippers have not reached the designated positions, either the threshold positions for grasping or the destinations for releasing. The path planner processes the position information in the global O_{XYZ} coordinate, and convert it into the (r, ϕ, θ, P_C) coordinates so that the formation controller recognizes it. Overall, the upper layer path planner monitors the positions

of the microgrippers and cargoes and decides the next action of the microgrippers.

Lower layer — formation, grasp and release sequence

The lower layer is formed based on the information received from the upper layer and synthesizes the appropriate global magnetic field input \mathbf{b}_a to realize the request. In a clockwise order, Fig. 8(A) displays two microgrippers which are initially open in the absence of field. They get closed and aligned with the applied field \mathbf{b}_a in (B) as soon as we turn on the field. The microgrippers are lifted in order to avoid disturbing cargoes in close proximity and therefore make grasping easier. The formation controller is then engaged autonomously at this point so that agents can adjust their positions locally through their inter-agent forces and globally through the applied magnetic field pulling action. Accordingly, the agents follow the designated path moving toward cargoes (C). For secure grasping, the inter-agent controller enables the microgrippers to arrive close enough to cargoes within a certain threshold distance away, see (D). When both microgrippers appear right above their respective cargoes, the global magnetic field \mathbf{b}_a is removed and triggered by a manual input. As a result, both microgrippers open and descend, landing on the cargoes, see (E). The timing of this action can be decided either by setting a fixed time period, distance metric-based automatic tracking, manual monitoring, or a combination of them which is used in this work as a proof-of-concept.

In the following step, the microgrippers are then closed by restoring the magnetic field \mathbf{b}_a without field gradient to grasp cargoes, rotate from $-z$ to $+z$, open, and then close again, see (F). This re-grasping action lets the cargoes, which are originally grasped by the tips of the microgrippers, fall into the hug of the microgrippers for secure grasping, reducing the possibility of losing cargoes during the following transportation. After collecting cargoes, the inter-agent formation control loop will be re-activated autonomously so that grippers can carry cargoes toward the final destination, see (G). Once the microgrippers arrive at the final destination, the releasing sequence takes place simply by removing the magnetic field \mathbf{b}_a and the microgrippers will both open to release cargoes to their goal positions, see (H).

The underlying system has nonholonomic motion due to the nonlinearity that exists in the generation of inter-agent forces as well as the underactuated pulling action associated to tri-axial Helmholtz coil system. Therefore, it is required to prescribe the motion of two microgrippers to follow path with intermediate moving goals (marked in yellow circles in Fig. 8). These moving goals are linearly constructed based on two subsequent original waypoint goals to avoid any sudden jumps in agents' motion.

The inter-agent force control method proposed in this paper has full capability to accomplish an arbitrary 3D configuration in close proximity. However, performing the 3D team cargo delivery experiment may not be as straightforward as the 2D one (Zhang et al. 2018) or the 3D one with particles, due to the fact that microgrippers have larger size and mass than individual particles. To succeed in the gripping experiment, the maximum polar inter-agent force needs to be made stronger than the apparent weight difference between each pair of agents of the team. To enlarge the range of motion on this demo, it just needs to make agents more neutrally buoyant by adding glass beads on top of the grippers' backpacks, and

increase the magnetization of each agent. Future research could enhance the 3D performance further by studying the dynamics of system to predict and avoid possible system nonlinear perturbations due to fluid interaction and gravity.

5.3 *Controllers performance assessment: P-controller versus optimization-based controller*

As explained in section 3.6, we augmented the definition of our inter-agent P-control method introduced in algorithm 1 in the form of an optimization-based control method, potentially capable to control more agents. This section will provide a comparative study between the P-controller and the OBC introduced in section 3.6. Video is available in supplementary materials showing the comparison demo for both controllers.

To assess the performance of each controller, three trials are executed whereby two agents follow a 3D path, which projects to the University of Toronto initials "UT" at top-view and a sharp corner line at side-view, as illustrated in Fig 9 (A) and only sketched for the best trial associated with the OBC. This image reflects how the paths are exactly seen through the top and side cameras with different zoom scales and offsets over the x -axis. The Root Mean Square error (RMS) between positions of agents and their corresponding intermediate goal waypoints is calculated. The study implies that the OBC with RMS error of $141 \mu\text{m}$ (\approx one fifth of the agents' body diameter) slightly outperforms the P-controller with RMS error of $165 \mu\text{m}$. The OBC renders a smoother tracking stability especially at sharp edges. The reason is that despite the self-tuning P-controller, the controller is synthesized based on a reference model including multiple regulator parameters. One of these parameters is slope convergence which patterns the motion of agents.

The corresponding time response of the local states $\bar{\mathbf{x}}_{\text{local}} = [r \ \phi \ \theta]^T$ along with the control input angles ψ and α are illustrated in Fig 9(B). The flipping behavior of these two angles to maintain the separation vector at desired orientation is evident. Last, Fig 9(C) illustrates how the gradient descent algorithm chooses the steepest direction to find the downhill global minimum traced in red-green dot sequence for the candidate sample at $t = 7\text{s}$. The corresponding optimal angle pair solution obtained by the OBC at $(13.8^\circ, 13.4^\circ)$ and declared by red square leads to a smoother motion as supposed to the near-optimal solution obtained by the P-controller at $(0^\circ, 0^\circ)$ and declared by yellow diamond.

6 Discussions and Conclusions

We have introduced a method to achieve, for the first time, independent position control of two functional magnetic microrobots levitating in 3D. We accomplished this through the use of magnetic inter-agent forces, which allows a team of microrobots to get into desired formations even while sharing a single global input magnetic field. The method was analyzed through simulation and experimental results, and shown to be viable to independently position each microrobot and move along arbitrary trajectories. Experimental results showed precise path following with two sets of microrobots including spherical and functional microgrippers along arbitrary paths in 3D. The close-proximity control of magnetic microrobots can

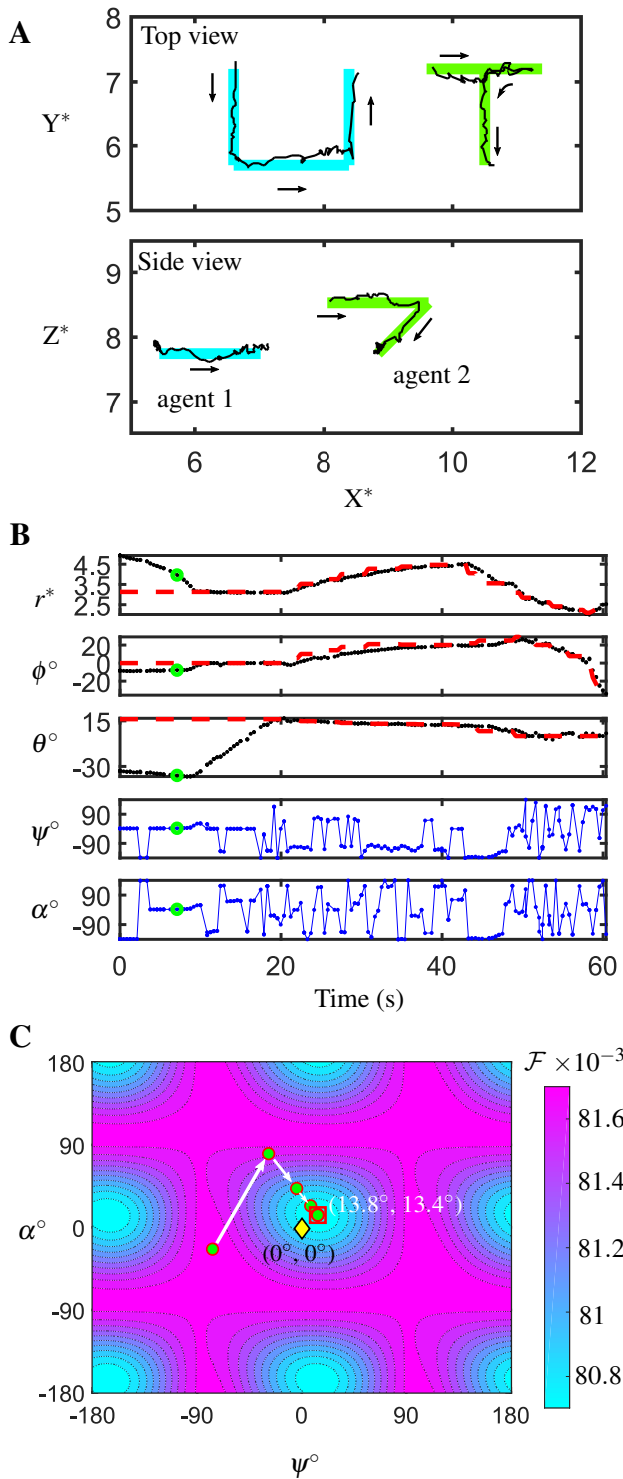


Fig. 9. Comparative study between optimization-based controller and P-controller: (A) 3D experimental result of two agents following a “UT” path at top-view and sharp corner line path at side-view. For simplicity, only the result belonging to the optimization-based controller is shown here. (B) Time response tracking of the local states and control inputs (red and black graphs refer to the desired and actual local state signals, respectively). (C) Gradient descent steepest search (red-green dot trace) utilized by the optimization algorithm to find the optimal control inputs solution is shown at the candidate time of $t = 7$ s and marked by green circle in (B). This optimal solution corresponds to the global minimum of the fitness function \mathcal{F} marked by the red square. For comparison, the near-optimal solution obtained by the P-controller is also displayed by yellow diamond.

be used for localized targeted drug delivery and field-activated medical devices.

We devised the method of inter-agent forces originally for the motion control of mobile multi-agent system of microrobots. Nevertheless, there are many design platforms where the proposed inter-agent force actuation idea could be applied to such as building a multi-model actuator by constraining the reciprocating inter-agent motion in the desired direction; for instance, one could use the radial force in the design of 1-DOF prismatic translation slider mechanism for drug injection or absorption (Salmanipour and Diller 2018); or one could apply the inter-agent rotations to enable team torque to be transduced to rotate a microvalve. Particularly, the biomedical applications connected to this work turns out to be in agreement with the emphasis on the small size requirement that can be accomplished using our method.

Given that our local inter-agent control law only relies upon the orientation of the magnetic field, the technique can be employed in combination with other magnetic actuation methods using time sequences such as rotating or oscillating magnetic fields, for example in swimming microrobots. One could employ two microgrippers as if using two hands.

One limitation of the proposed method in this paper is that the orientation of each microrobot cannot be controlled independently. However, one can potentially study the inter-agent forces between pairs of agents in an analogous way to this work but for a more general case where an arbitrary nonuniform field can be patterned across the workspace. Each agent would then experience a slightly different field, and hence the orientation of each agent could be programmed independently in a predictive manner. In this respect, the quantity of discrete magnetic generators inputs should be chosen such that it maintains a full rank system matrix to allow for independent actuation of all possible desired DOFs. These field generator inputs could be either coil currents or permanent magnets motion DOFs. To this end, at least $5 \times n$ field generator inputs are needed for a pair of agents that can be fully controlled in their pos , 3 for independent position control and 2 for independent heading control associated to each agent.

This study shows that even though the magnetic gradient pulling action was constrained due to the coil design used, we still were able to accomplish independent position control of two microrobots using a common laboratory tri-axial Helmholtz coil system readily available. Thus, it is expected to get even better result by utilizing a fully actuated coil system for a homogeneous field generation such as the Octomag system.

Due to inertia-less behavior of our microrobots at low Reynolds number environments, we did not analyze the impact of dynamics in this study. A dynamic treatment of the multi-agent system in close proximity that can adjust the dynamics between one configuration to another is left as future research. One can also utilize the presented framework for soft-body (flexible) microrobots, where more DOFs can result in features such as more advanced locomotion patterns. Another avenue for future research is to explore the nonlinear controllability of the internal states \bar{x}_{local} . To this end, the problem could be formulated using Lie brackets to investigate

the independent directions of motion based on the local control inputs ψ and α .

Funding

This research was supported by the Natural Sciences and Engineering Research Council of Canada (NSERC) through the Discovery Grant Program (grant number 2014-04703).

References

- Abbott J, Diller E and Petruska A (2020) Magnetic methods in robotics. *Annu. Rev. Control Robot. Auton. Syst.* 3.
- Abbott JJ, Brink JB and Osting B (2017) Computing minimum-power dipole solutions for interdipole forces using nonlinear constrained optimization with application to electromagnetic formation flight. *IEEE Robotics and automation letters* 2(2): 1008–1014.
- Becker A, Onyuksel C, Bretl T and McLurkin J (2014) Controlling many differential-drive robots with uniform control inputs. *The international journal of Robotics Research* 33(13): 1626–1644.
- Ceylan H, Giltinan J, Kozielski K and Sitti M (2017) Mobile microrobots for bioengineering applications. *Lab on a Chip* 17(10): 1705–1724.
- Choi K, Salehizadeh M, Da Silva RB, Hakimi N, Diller E and Hwang DK (2017) 3d shape evolution of microparticles and 3d enabled applications using non-uniform uv flow lithography (nuf). *Soft matter* 13(40): 7255–7263.
- Chowdhury S, Jing W and Cappelleri DJ (2015) Controlling multiple microrobots: recent progress and future challenges. *Journal of Micro-Bio Robotics* 10(1-4): 1–11.
- Chowdhury S, Johnson BV, Jing W and Cappelleri DJ (2017) Designing local magnetic fields and path planning for independent actuation of multiple mobile microrobots. *J. Micro-Bio Robot.* 12(1): 21–31.
- Diller E, Floyd S, Pawashe C and Sitti M (2011) Control of multiple heterogeneous magnetic microrobots in two dimensions on nonspecialized surfaces. *IEEE Transactions on Robotics* 28(1): 172–182.
- Diller E, Giltinan J, Lum GZ, Ye Z and Sitti M (2016) Six-degree-of-freedom magnetic actuation for wireless microrobotics. *The International Journal of Robotics Research* 35(1-3): 114–128.
- Diller E, Giltinan J and Sitti M (2013) Independent control of multiple magnetic microrobots in three dimensions. *The International Journal of Robotics Research* 32(5): 614–631.
- Dong X and Sitti M (2020) Controlling two-dimensional collective formation and cooperative behavior of magnetic microrobot swarms. *The International Journal of Robotics Research* : 0278364920903107.
- Elhebeary M and Saif MTA (2017) Lessons learned from nanoscale specimens tested by mems-based apparatus. *Journal of Physics D: Applied Physics* 50(24): 243001.
- Floyd S, Diller E, Pawashe C and Sitti M (2011) Control methodologies for a heterogeneous group of untethered magnetic micro-robots. *The International Journal of Robotics Research* 30(13): 1553–1565.
- Howell TA, Osting B and Abbott JJ (2018) Sorting rotating micromachines by variations in their magnetic properties. *Physical Review Applied* 9(5): 054021.
- Huang TY, Qiu F, Tung HW, Peyer KE, Shamsudhin N, Pokki J, Zhang L, Chen XB, Nelson BJ and Sakar MS (2014) Cooperative manipulation and transport of microobjects using multiple helical microcarriers. *Rsc Advances* 4(51): 26771–26776.
- Johnson BV, Chowdhury S and Cappelleri D (2020) Local magnetic field design and characterization for independent closed-loop control of multiple mobile microrobots. *IEEE/ASME Transactions on Mechatronics* .
- Kaiser A, Snezhko A and Aranson IS (2017) Flocking ferromagnetic colloids. *Science advances* 3(2): e1601469.
- Kantaros Y, Johnson BV, Chowdhury S, Cappelleri DJ and Zavlanos MM (2018) Control of magnetic microrobot teams for temporal micromanipulation tasks. *IEEE Transactions on Robotics* 34(6): 1472–1489.
- Khalil IS, Tabak AF, Hamed Y, Tawakol M, Klingner A, El Gohary N, Mizaikoff B and Sitti M (2018) Independent actuation of two-tailed microrobots. *IEEE Robotics and Automation Letters* 3(3): 1703–1710.
- Kokot G, Piet D, Whitesides GM, Aranson IS and Snezhko A (2015) Emergence of reconfigurable wires and spinners via dynamic self-assembly. *Scientific reports* 5: 9528.
- Kummer MP, Abbott JJ, Kratochvil BE, Borer R, Sengul A and Nelson BJ (2010) Octomag: An electromagnetic system for 5-dof wireless micromanipulation. *IEEE Transactions on Robotics* 26(6): 1006–1017.
- Li S, Batra R, Brown D, Chang HD, Ranganathan N, Hoberman C, Rus D and Lipson H (2019) Particle robotics based on statistical mechanics of loosely coupled components. *Nature* 567(7748): 361–365.
- Mahoney AW and Abbott JJ (2016) Five-degree-of-freedom manipulation of an untethered magnetic device in fluid using a single permanent magnet with application in stomach capsule endoscopy. *The International Journal of Robotics Research* 35(1-3): 129–147.
- Miyashita S, Diller E and Sitti M (2013) Two-dimensional magnetic micro-module reconfigurations based on inter-modular interactions. *Int. J. Robot. Res.* 32(5): 591–613.
- Ongaro F, Pane S, Scheggi S and Misra S (2019) Design of an electromagnetic setup for independent three-dimensional control of pairs of identical and nonidentical microrobots. *IEEE transactions on robotics* 35(1): 174–183.
- Petruska AJ and Nelson BJ (2015) Minimum bounds on the number of electromagnets required for remote magnetic manipulation. *IEEE Transactions on Robotics* 31(3): 714–722.
- Rahmer J, Stehning C and Gleich B (2017) Spatially selective remote magnetic actuation of identical helical micromachines. *Science Robotics* 2(3): eaal2845.
- Rubenstein M, Cornejo A and Nagpal R (2014) Programmable self-assembly in a thousand-robot swarm. *Science* 345(6198): 795–799.
- Salehizadeh M and Diller E (2016) Two-agent formation control of magnetic microrobots. In: *International Conference on Manipulation, Automation and Robotics at Small Scales*. IEEE, pp. 1–6.
- Salehizadeh M and Diller E (2017a) Optimization-based formation control of underactuated magnetic microrobots via inter-agent forces. In: *International Conference on Manipulation, Automation and Robotics at Small Scales*. IEEE, pp. 1–5.

- Salehizadeh M and Diller E (2017b) Two-agent formation control of magnetic microrobots in two dimensions. *Journal of Micro-Bio Robotics* 12(1-4): 9–19.
- Salehizadeh M, Li Z and Diller E (2019) Independent position control of two magnetic microrobots via rotating magnetic field in two dimensions. In: *International Conference on Manipulation, Automation and Robotics at Small Scales*. IEEE, pp. 1–6.
- Salehizadeh M, Salmanipour S, Zhang J and Diller E (2018) Controlling multiple microrobots using homogeneous magnetic fields. In: *IEEE International Conference on Robotics and Automation (workshop paper)*. DOI: 10.13140/RG.2.2.25638.27201/2, pp. 1–5.
- Salmanipour S and Diller E (2018) Eight-degrees-of-freedom remote actuation of small magnetic mechanisms. In: *IEEE International Conference on Robotics and Automation*. pp. 1–6.
- Tottori S, Zhang L, Peyer KE and Nelson BJ (2013) Assembly, disassembly, and anomalous propulsion of microscopic helices. *Nano letters* 13(9): 4263–4268.
- Wang Q, Yang L, Wang B, Yu E, Yu J and Zhang L (2018) Collective behavior of reconfigurable magnetic droplets via dynamic self-assembly. *ACS applied materials & interfaces* 11(1): 1630–1637.
- Wong D, Steager EB and Kumar V (2016) Independent control of identical magnetic robots in a plane. *IEEE Robotics and Automation Letters* 1(1): 554–561.
- Xie H, Sun M, Fan X, Lin Z, Chen W, Wang L, Dong L and He Q (2019) Reconfigurable magnetic microrobot swarm: Multimode transformation, locomotion, and manipulation. *Science Robotics* 4(28): eaav8006.
- Xu T, Zhang J, Salehizadeh M, Onaizah O and Diller E (2019) Millimeter-scale flexible robots with programmable three-dimensional magnetization and motions. *Science Robotics* 4(29): eaav4494.
- Yesin KB, Vollmers K and Nelson BJ (2006) Modeling and control of untethered biomicrobots in a fluidic environment using electromagnetic fields. *The International Journal of Robotics Research* 25(5-6): 527–536.
- Yu J, Wang B, Du X, Wang Q and Zhang L (2018) Ultra-extensible ribbon-like magnetic microswarm. *Nature communications* 9(1): 3260.
- Yu W, Lin H, Wang Y, He X, Chen N, Sun K, Lo D, Cheng B, Yeung C, Tan J et al. (2020) A ferrobatic system for automated microfluidic logistics. *Science Robotics* 5(39).
- Zhang J, Salehizadeh M and Diller E (2018) Parallel pick and place using two independent untethered mobile magnetic microgrippers. In: *IEEE International Conference on Robotics and Automation*. IEEE, pp. 123–128.
- Zhang Z, Long F and Menq CH (2012) Three-dimensional visual servo control of a magnetically propelled microscopic bead. *IEEE Transactions on Robotics* 29(2): 373–382.

Appendix A. Stability proof

This appendix provides stability proof for the adaptive P-controller applied to two-agent configuration in this paper.

A.1 Assumptions

1. The inertia is negligible for the underlying system.

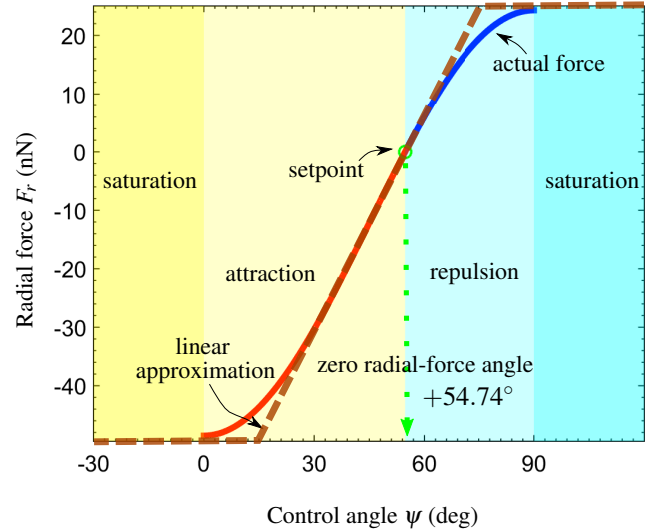


Fig. 10. Linear approximation of the radial force at the setpoint $x^* = (r = r_{\text{des}}, \psi = 54.74^\circ, \alpha = 54.74^\circ)$. For simplicity, only one control angle axis is shown corresponding to Fig. 3(A).

2. As the separation error increases, the P-controller will be saturated converting to a bang-bang controller which takes the highest convergence rate.
3. Using Taylor approximation, the nonlinear radial force function can be replaced with a linear model up to the saturation as illustrated in Fig. 10.
4. We model system to be time-invariant.

Here, our trajectory is a single setpoint and we aim to prove that using P-controller the closed-loop system will be globally asymptotically stable about the desired setpoint at $x^* = (r = r_{\text{des}}, \psi = 54.74^\circ, \alpha = 54.74^\circ)$ within the interaction zone of the pair of agents. To this end, Lyapunov's direct stability method is applied to two system models:

1. First-order ODE without inertia
2. Second-order dynamics including inertia

The dominant state we are concerned about is the separation $x = r$. Without loss of generality, we consider the scaled radial inter-agent force as the input to the system denoted by $u(\psi) = -\frac{f_r}{\sigma} = -\frac{\Omega}{\sigma x^4} [1 - 3 \cos^2 \psi \cos^2 \alpha]$ based on (4a). Now let's check out the stability for the two models:

A.2 First-order ODE without inertia

The closed-loop equation has the following form,

$$x^4 \dot{x} = u'(\psi), \quad (22)$$

where $u' = x^4 u$.

Fig. 10 shows the feasibility to approximate the radial force by a linear model at the setpoint to justify the usage of the P-corrector. Hence, $u' = -Ke$, and $K > 0$ denotes the gain of the P-controller.

Lemma 2. *Using P-controller the closed-loop system (22) is globally asymptotically stable at the setpoint x^* within the interaction zone of the pair of agents.*

Proof. Choose a positive definite quadratic Lyapunov's candidate as $V(\tilde{x}) = \frac{1}{2}\tilde{x}^T K\tilde{x}$, where $\tilde{x} = x - r_{\text{des}}$. For the sake of simplicity, here after we will represent \tilde{x} by x . Then,

$$\dot{V} = \dot{x}^T Kx = -\dot{x}^T x^4 \dot{x}, \quad (23)$$

will be negative semi-definite. Appeal to LaSalle's principle: find the largest invariant set constrained in $S = \{(x, \dot{x}) : \dot{x} = 0\}$. Using eq. (22), $\dot{x} = 0 \rightarrow Ke = 0 \rightarrow x = 0$. Therefore, the largest invariant set is same as the setpoint. Consequently, the closed-loop system is globally asymptotically stable at the setpoint x^* . The global property is because $V \rightarrow \infty$ as $\|x\| \rightarrow \infty$. ■

A.3 Second-order dynamics including inertia

We used Euler-Lagrange formula to derive the Hamiltonian form of Newton's equation for the underlying system given as,

$$L(q, \dot{q}) = T - U : \frac{d}{dt} \frac{\partial L}{\partial \dot{q}} - \frac{\partial L}{\partial q} = \tau \quad (24)$$

where \dot{q} is the generalized velocity vector and $\tau = 2f_r - b\dot{r}$ is the generalized force including Rayleigh dissipation functions which are magnetic and fluid drag friction (damping) forces here.

Solving the above equation, it carries forward the closed-loop equation as,

$$\begin{aligned} Mx^4 \ddot{x} + b(\dot{x}, x)x^4 \dot{x} &= u'(\psi), \\ u'(\psi) &= 1 - 3\cos^2(\psi)\cos^2(\alpha). \end{aligned} \quad (25)$$

Let $u'(\psi) = -Ke = -Kx$. Microagent's mass and fluid drag constant are denoted by M and b , respectively.

Lemma 3. *Using P-controller the closed-loop system (25) is globally asymptotically stable at the setpoint x^* within the interaction zone of the pair of agents.*

Proof. We choose the total energy of the system as our quadratic Lyapunov's function as,

$$V(x, \dot{x}) = \frac{1}{2}\dot{x}^T Mx^4 \dot{x} + \frac{1}{2}x^T Kx. \quad (26)$$

The function V is positive definite and decrescent. Let's calculate \dot{V} along trajectory 25. After some modifications we will have,

$$\dot{V} = -\dot{x}^T bx^4 \dot{x} + \frac{1}{2}\dot{x}^T (\dot{M}x^4 + 4Mx^3)\dot{x}, \quad (27)$$

assuming $\dot{M} = 0$, the second term on the right side of eq. (27) is negligible against the first term because the inertia is insignificant. Hence, $\dot{V} = \dot{x}^T bx^4 \dot{x} \leq 0$. Using LaSalle's principle similar to previous section one can prove that the closed-loop system is globally asymptotically stable at the setpoint x^* . The global property is because $V \rightarrow \infty$ as $\|x\| \rightarrow \infty$.

One can make the same strategy above to prove Lyapunov stability of the closed-loop system for the pair heading states ϕ and θ , under the act of switching Relay nonlinear controller. In this respect, the sinusoidal relation between the angular forces and the control angles (see Fig. 3(B,C)) needs to be approximated with a line around the set point. ■

Appendix B. Index to Multimedia Extensions

The multimedia extensions to this article are at <http://www.ijrr.org>.

Table of Multimedia Extensions

Extension	Type	Description
1	Video	The single video file includes physics-based animations and experimental demonstrations.